

536541

A study of the response of deep tropical clouds to mesoscale processes: Part I: Modeling strategies and simulations of TOGA-COARE convective systems.

D. E. Johnson¹, W.-K. Tao², J. Simpson², and C.-H. Sui²

¹Goddard Earth Sciences and Technology Center
University of Maryland, Baltimore County
Baltimore, MD

²Laboratory for Atmospheres
NASA/Goddard Space Flight Center
Greenbelt, MD 20771

Journal of the Atmospheric Sciences

(February 27, 2001)

Corresponding author address: Dr. Daniel E. Johnson, Mesoscale Atmospheric Processes
Branch, Code 912, NASA/GSFC, Greenbelt, MD 20771
Email: djohnson@agnes.gsfc.nasa.gov

Abstract

Interactions between deep tropical clouds over the western Pacific warm pool and the larger-scale environment are key to understanding climate change. Cloud models are an extremely useful tool in simulating and providing statistical information on heat and moisture transfer processes between cloud systems and the environment, and can therefore be utilized to substantially improve cloud parameterizations in climate models. In this paper, the Goddard Cumulus Ensemble (GCE) cloud-resolving model is used in multi-day simulations of deep tropical convective activity over the Tropical Ocean-Global Atmosphere Coupled Ocean-Atmosphere Response Experiment (TOGA COARE). Large-scale temperature and moisture advective tendencies, and horizontal momentum from the TOGA-COARE Intensive Flux Array (IFA) region, are applied to the GCE version which incorporates cyclical boundary conditions. Sensitivity experiments show that grid domain size produces the largest response to domain-mean temperature and moisture deviations, as well as cloudiness, when compared to grid horizontal or vertical resolution, and advection scheme. It is found that a minimum grid-domain size of 500 km is needed to adequately resolve the convective cloud features. The control experiment shows that the atmospheric heating and moistening is primarily a response to cloud latent processes of condensation/evaporation, and deposition/sublimation, and to a lesser extent, melting of ice particles. Air-sea exchange of heat and moisture is found to be significant, but of secondary importance, while the radiational response is small. The simulated rainfall and atmospheric heating and moistening, agrees well with observations, and performs favorably to other models simulating this case.

1. Introduction

The physical complexity and nonlinearity of interactions between deep convective cloud systems and the large-scale environment is one of the key uncertainties in understanding climate change. Cloud systems, especially over the warm tropical waters of the western Pacific and east Indian oceans, largely influence atmospheric radiative heating, as well as air-sea interactions due to latent and sensible heat release. A good correlation of greater atmospheric heating exists over these warm pool regions, which has the importance of setting atmospheric global-heating gradients, and thus greatly influences the general circulation of the atmosphere. However the importance of the air-sea and radiative energy transfers due to the cloud systems, and the coupling of the energy transfer from tropical precipitating cloud systems to the large-scale energy budget, remains poorly understood, and must be more fully understood before the accuracy of climate and General Circulation Models (GCMs) can be substantially improved. The need for a better understanding of the coupling between the ocean and atmosphere, and the principal atmospheric processes that organize convection over the western Pacific warm pool, were major initiatives for the design of the Tropical Ocean-Global Atmosphere Coupled Ocean-Atmosphere Response Experiment (TOGA COARE; Webster and Lukas, 1992).

Observations taken from TOGA-COARE, representing both local and large-scale averages, have been utilized by such studies as the Global Energy and Water-Cycle Experiment (GEWEX) Cloud System Study (GCSS 1993) to develop and validate cloud-resolving models with the ultimate goal of developing more accurate cloud-scale parameterizations (in this case deep tropical clouds) for climate and GCM models. Since even high-resolution GCMs, with typical grid sizes less than 100 km, cannot resolve the individual convective cells of accompanying mesoscale circulations in a grid box, the approach of the GCSS is to utilize cloud-resolving models (CRMs) to explicitly resolve and quantify the collective effects of individual clouds while at the same time, encompassing the entire cloud system within a single GCM column. Thus the CRM can be used to quantify the cumulative large-scale effects of cloud systems, and to examine the role in which large-scale processes relate to the development, maintenance, and structure of deep convective cloud systems.

Working Group 4 of the GCSS (GCSS WG4) has the specific role of understanding the behavior of deep precipitating convective cloud systems (Moncrieff et al. 1997), and has conducted four studies as of this writing (Cases 1-4). Case 2 of the GCSS WG4 (Krueger and Lazarus 1999) has involved the study of deep tropical convection during the active period of 19-27 December 1992, over the Intensive Flux Array (IFA) region of the TOGA-COARE experiment (Fig. 1). Several CRMs are participating in this project and descriptions and details of them can be found in Krueger and Lazarus (1999). The CRM has evolved significantly in the study of cloud-environment interactions over the past two decades. With the inclusion of large-scale momentum, and temperature and moisture advective forcings into the CRM, a response of a population or an ensemble (CRM can also be denoted as Cloud Ensemble Model; CEM) of clouds to the large-scale forcings, and the statistical properties of the cloud systems, can be obtained using cyclical boundaries, relatively large horizontal domains (> 500 km), and high resolutions (< 2 km). The evolution of the ensemble (CRM) approach since the early development by Soong and Ogura (1980), including the developers and models involved, is depicted in Table 1. Over the last 20 years these models have become increasingly sophisticated through the introduction of detailed microphysical process, radiation and boundary-layer effects, and improved turbulent parameterizations for subgrid-scale processes. In addition, exponentially increasing computer resources have resulted in time integrations increasing from hours to days, domain grids boxes increasing from < 2000 to $> 2\,500\,000$, and 3-D models becoming increasingly prevalent. The CRM is now at a stage where it can provide reasonably accurate statistical information of the sub-grid, cloud resolving processes now poorly parameterized in climate models.

One objective of this paper is to examine the role in which the model numerics and grid setup plays in the development and structure of deep tropical convection, when large-scale momentum, temperature, and moisture advective forcings are applied. In addition, this paper will examine the heat and moisture budgets, as well as precipitation for a control simulation over the entire domain, and in convective and stratiform regions. This will include studying the individual components which make up the heating and moistening budgets. A brief description of the GCE CEM model is provided in section 2. Large-scale observations, their application to the GCE, and the experimental design and model setup are presented in section

3. Section 4 presents a number of sensitivity experiments that examine the effects of model domain size, grid resolution, and model numerics on the simulated thermodynamics and dynamics of the simulated events. Here special emphasis is given on the causes of relatively large mean temperature and moisture errors as a function of domain size. Section 5 presents results from the control simulation, including a convective-stratiform breakdown of the dynamics and thermodynamics for this case. Finally a summary and discussion of results are presented in section 6.

2. Model description

The CRM used in this study is the two-dimensional version of the Goddard Cumulus Ensemble (GCE) model, and is primarily documented in Tao and Simpson (1993). Some recent improvements to the GCE include the addition of a detailed 4-ice scheme (Ferrier 1994, Ferrier et al. 1995), a positive-definite advection scheme (Tao et al. 1996), a TOGA-COARE surface flux algorithm (Wang et al. 1996) and a PLACE model surface parameterization (Lynn et al. 1998). These improvements to the GCE have resulted in a number of different physical parameterizations that can be utilized for the study of cloud microphysics, advection, surface, and radiation processes at cloud-resolving scales. The model so far has been extensively applied to explicitly represent cloud-environment interactions, cloud-cloud interactions and mergers, cloud-radiation interactions, air-sea interactions, cloud draft structures, and trace gas transport (a review is given by Simpson and Tao, 1993).

A brief summary of the model configuration for this study is now presented. The equations that govern cloud-scale motion (wind) are anelastic by neglecting the local variation of air density with time in the mass continuity equation (see Tao and Soong, 1986 for a description of the anelastic assumption and cloud motion equations). The subgrid-scale turbulence (one-and-a-half order) scheme used in the GCE model is based on work by Klemp and Wilhelmson (1978), and Soong and Ogura (1980). In their approach, one prognostic equation is solved for the subgrid kinetic energy, which is then used to specify the eddy coefficients. The effect of condensation on the generation of subgrid-scale kinetic energy is also incorporated in the model (Tao and Soong, 1986). The cloud microphysics includes a

parameterized Kessler-type two-category liquid water scheme (cloud water and rain), and a parameterized Lin et al. (1983) or Rutledge and Hobbs (1984) three-category ice-phase scheme (cloud ice, snow and hail/graupel; Tao et al., 1993). Shortwave (solar) and longwave (infrared) radiation parameterizations described by Chou (1984, 1986, 1990, 1992) are also included in the model. The GCE model has recently implemented a Multi-dimensional Positive Definite Advection Transport Algorithm (MPDATA; Smolarkiewicz, 1983, 1984) scheme with a non-oscillatory option (Smolarkiewicz and Grabowski, 1990). All scalar variables (potential temperature, water vapor, turbulence coefficient and all five hydrometeor classes) use forward time differencing and the MPDATA for advection. The MPDATA can only advect those variables which are either all positive or all negative. Since the dynamic variables (u , v and w) can be positive or negative, a second-order accurate advection scheme, and leapfrog time scheme which semi-conserves kinetic energy, is used for these variables.

3. Observations and design of the numerical experiments

a. Temperature, moisture, and momentum forcings

The case chosen for this experiment is the 19-27 December 1992, multi-day period of TOGA-COARE (Webster and Lukas, 1992), which is the same period utilized by the GCSS WG4 Case 2 experiment discussed in section 1. This case evolved during the developing phase of a westerly wind burst that occurred over the TOGA-COARE Intensive Flux Array (IFA; Fig. 1) and is described in more detail in Krueger and Lazarus (1999).

For the simulations presented in this study, the observed large-scale advective tendencies of potential temperature, water vapor mixing ratio, and horizontal momentum are used as the main large-scale forcings which govern the GCE model in a semi-prognostic manner (Soong and Ogura, 1980; Soong and Tao, 1980). These are applied uniformly over the model domain with the assumption of the model domain being much smaller than the large-scale disturbances. The major characteristics of this approach are that ensembles of clouds can be generated by using the "observed-prescribed forcings". The large-scale advective tendencies for potential temperature θ , and water vapor mixing ratio q_v are defined as:

$$\left(\frac{\partial \bar{\theta}}{\partial t} \right)_{\text{L.S.}} = -\bar{\mathbf{v}} \cdot \nabla \bar{\theta} - \bar{w} \frac{\partial \bar{\theta}}{\partial z} \quad (1)$$

and

$$\left(\frac{\partial \bar{q}}{\partial t} \right)_{\text{L.S.}} = -\bar{\mathbf{v}} \cdot \nabla \bar{q} - \bar{w} \frac{\partial \bar{q}}{\partial z} \quad (2)$$

where L.S. denotes IFA-averaged (approximately 500 km x 500 km) values.

Since accurate calculations of the large-scale horizontal momentum forcing terms are difficult to obtain from observations in the tropics, these terms are instead replaced by a nudging term:

$$\left(\frac{\partial \bar{\mathbf{v}}}{\partial t} \right)_{\text{L.S.}} = -\frac{\bar{\mathbf{v}} - \bar{\mathbf{v}}_{\text{obs}}}{\tau} \quad (3)$$

where $\bar{\mathbf{v}}$ is the predicted large-scale horizontal velocity, $\bar{\mathbf{v}}_{\text{obs}}$ is the observed large-scale horizontal velocity, and τ is the specified adjustment time scale of approximately one hour (Grabowski et al. 1996, Xu and Randall 1996b). This method constrains the domain-averaged horizontal velocities to follow the observed values, and thereby provides a simple means in controlling the cloud system dynamics by the large-scale momentum and shear.

b. Observed thermodynamic and dynamic fields

The IFA-averaged profiles of temperature, moisture, vertical velocities, and horizontal wind fields and forcings, were provided every six hours at 25 mb intervals from 1000 to 75 mb from the TOGA-COARE diagnostic analyses of Lin and Johnson (1996). A depiction of the IFA-mean u-wind field (Fig. 2a) shows increasing westerly zonal flow from 5 to 13 m s⁻¹ below 500 mb, and increasing easterly winds from 5 to 20 m s⁻¹ above 300 mb from 19-23 December. The v-wind field (Fig. 2b) indicates increasing southerly flow above 300 mb from 5 to 13 m s⁻¹ during this same period, with weaker northerly winds between 400 and 600 mb. An additional increase in the mean wind shear occurs again after 25 December. The wind shear directly impacts the structure and organization of the cloud systems, as well as the

extents of heat and moisture transfer from the ocean to atmosphere, and would be conducive to convective organization during this period. The IFA-mean vertical velocity field (Fig. 2c) shows that there are five convective episodes concurrent during this period. The first three occur during the period of increasing shear between 20 and 23 December, while the fourth exists just prior to the second period of deepening shear on 24 December. The fourth event is the strongest, as indicated by maximum mean updrafts of 13 cm s^{-1} between 300 and 400 mb, versus 6 to 9 cm s^{-1} at similar levels for the first three events. The last or fifth event occurs near the end of the simulation on 27 December, and is weaker than the others.

The temperature advective forcing field (Fig. 3a) also shows the five convective events producing maximum heating rates in the middle atmosphere between 400 and 600 mb. The maximum advective heating rate of 46 K day^{-1} occurs during the fourth event, late on 24 December near the region of maximum updraft at 450 mb. Weaker heating rates of 20 to 35 K day^{-1} occur 50 to 100 mb lower, with the exception of the third event. Similarly, the moisture advective forcing profile (Fig. 3b) indicates maximum atmospheric drying in the mid-troposphere, with a discontinuity in moistening during the fifth event. Because this last event is the weakest and least developed, this paper will focus primarily on the first four events. Strong atmospheric moistening, mainly due to the evaporation of rain, does occur below 700 mb, but primarily after the large event on 25 December.

c. Experiment design and model setup

In this study, four experiments (A-D) are initially conducted in order to test the effects in which grid resolution, model domain size, and vertical filtering plays on the simulated cloud structure, environmental thermodynamics, heating and moistening budgets, radiation, surface fluxes, and rainfall amounts. This leads to a total of nine simulations, which are configured as shown in Table 2. Each simulation is setup identically, except for one characteristic advective, domain size, or grid spacing feature as highlighted in the table. Note that the four experiments have one simulation that is identical. This simulation, denoted as C512, consists of 512 horizontal points, a horizontal grid spacing of 1000 m, 41 vertical levels with vertical grid spacing ranging from 80 m near the surface to 1000 m near the top of the domain, and a

positive definite advection scheme. This setup is the same as that used in the GCSS WG4 case 2 study, and will be referred to as the 'control simulation' in this paper.

The purpose of experiment A is to examine the role of domain *size* on the mean distribution, structure, and evolution of deep tropical convection during this active period of TOGA COARE. Here the horizontal domain varies from 128 km to 1024 km, using a 1000 m grid spacing. Similar to A, experiment B examines the role of *horizontal grid resolution* on the simulated TOGA-COARE events, with grid spacings ranging from $dx=500$ to 2000 m, over a 512-km domain. Experiment C addresses the effects that *vertical grid resolution* plays on the simulations, by varying the number of vertical levels and spacing from 32 to 50, and from 50/750 m to 126/1200 m (bottom/top of domain) respectively. Finally, the purpose of experiment D is to better understand the role in which vertical filtering of the advective variables plays on the simulated results. In this experiment, simulation PDOFF uses a second-order vertical filter (Wilhelmson and Chen 1982), while VFILT4 uses a fourth-order numerical filter in the vertical direction. The control simulation does not use either of these vertical filters, but instead utilizes the positive-definite advection scheme as described in the next section.

All nine simulations in this study incorporate a modified 3-class Rutledge and Hobbs (1984) ice microphysics package as described in Tao et al. (1993), the full radiation package of Chou (1992) and Chou and Suarez (1994), and an aerodynamic surface flux air-sea interaction package. The lower-boundary of the model is represented by the ocean surface. Here the surface pressure and sea-surface temperature (SST) are averaged over the IFA and are provided at 6-hour intervals. The observed SST is then utilized by the GCE for surface latent and sensible heat flux calculations. Free-slip, rigid, bottom and top boundary conditions are applied together with a relaxation layer above 16 km to absorb gravity waves. In the horizontal, cyclic lateral boundary conditions are incorporated to ensure that there is no additional heat or moisture forcing inside the domain apart from the large-scale forcing (Soong and Tao 1980; Tao and Soong 1986). Since the IFA is located near the equator, the Coriolis term is neglected due to its insignificant effect on cloud- and mesoscale-scale circulations compared to the large-scale momentum nudging term. The simulations are initialized at 0000 UTC 19 December 1992 by using an IFA-averaged mean sounding

described in the previous section. The simulations are then integrated for eight days until 0000 UTC 27 December 1992, using a time step of 6 s. Convection is initiated by introducing small random perturbations in the temperature field (0.5 K magnitude maximum) in the sub-cloud layer during the first 150 minutes. The temperature, moisture, and horizontal momentum advective forcings are updated every six hours to observations, and linearly interpolated between updates.

4. Sensitivity Studies

a. Vertical advection scheme

The control case (C512), which uses a positive definite advection scheme (MPDATA; Smolarkiewicz 1983, Smolarkiewicz and Grabowski 1990) on all the scalar variables, is compared to a simulation using a standard 2nd-order vertical filter (PDOFF), and a simulation incorporating a 4th-order vertical filter (VFILT4) in experiment D. Figure 4 shows that the mean Q1 and Q2 rates have only small differences between the simulations, indicating that the energy budgets of the three schemes are consistent and primarily responding to the imposed large-scale forcings. In agreement to the latent heating profiles, there are only small differences in total rainfall, with the C512 simulation producing 161.6 mm (Table 3) which is in good agreement with observations (160.8 mm) and between the other cases. The hydrometeor structures and distributions, however, show major differences, depending on the vertical advection scheme used. Figure 5 shows that the PDOFF simulation has much more oscillation and small-scale disturbances in the mean hydrometeor fields, especially in the snow and graupel fields. The domain-averaged time-dependent snow fields for the three cases (Fig. 6) show that the MPDATA simulation (C512) fields are much smoother in the convective and stratiform regions, a characteristic which exists for nearly the entire simulation. The PDOFF simulation tends to overproduce peak domain-averaged values of the snow, graupel, and rain mixing ratios. Conversely, the simulation with the 4th-order vertical filter (VFILT4) produces hydrometeor fields which are nearly as smooth as the control

simulation, however the magnitudes of the mean hydrometeor fields for this case tend to be greater than in the MPDATA case.

The PDOFF simulation has the disadvantage of introducing negative values into the resulting advective solution for the hydrometeors, and then using the advective solution as input to the nonlinear equations describing the microphysical phenomena. This results in the "ripples" in the solution, which can eventually lead to instability of the whole system. The MPDATA scheme produces smoother, more realistic results, but requires iterations and thus needs more computational resources. As shown in this section, the VFILT4 scheme presents a good compromise between the traditional 4th-order advective (PDOFF), and MPDATA (C512) schemes. The VFILT4 results are smoother and similar to the MPDATA, the magnitudes are greater than MPDATA but less than PDOFF, and computational resources are similar to the PDOFF but much less than the MPDATA. Thus it is shown that the VFILT4 provides a feasible method in removing instabilities in the solutions and could be useful for time-consuming 3-D simulations. However, for the 2-D simulations in this paper, the more accurate MPDATA scheme is used.

b. Temperature and Moisture errors

Figures 7 and 8 show the domain and time-averaged temperature and water vapor mixing ratio deviations from the TOGA-COARE IFA observed values for experiments A-D. For all simulations, the temperature error profiles follow a similar pattern, with a mean temperature error below 300 mb near -2 K, and slightly warmer temperature deviations of -1.5 K near 600 mb. Above 300 mb, temperatures cool and approach near -6 K at 100 mb. Reasons for the larger errors near the tropopause are likely due to poor vertical resolution and incorrect prediction of the tropopause height as discussed in Grabowski et al. (1998). The moisture-error profiles also follow a similar pattern between the cases, with excess drying of about -0.5 g kg^{-1} below 900 mb, and moistening of about 0.5 g kg^{-1} in the midlevels. The mid-level moistening pattern resembles GATE simulations performed by Grabowski et al. (1998), and is likely attributed to insufficient moisture removal due to the periodic boundaries.

It is evident from these figures that the largest deviations of both temperature and moisture occur in the simulations that are dependent on domain size (Experiment A). Here mean temperature deviations between cases N128 and N1024 are near 1 K in the lower and upper troposphere, while errors are less than 0.2 K for the other experiments. For water vapor, mean deviations are near 0.6 g kg^{-1} between 700 to 900 mb in Experiment A, but less than 0.2 g kg^{-1} in the other experiments. Smaller errors in the temperature and moisture fields occur for the largest domain (N1024), which indicates that the response of the simulated thermodynamic state of the atmosphere is most dependent on domain size (Experiment A), in comparison to horizontal and vertical resolution (Experiments B and C), and numerical filtering (Experiment D). To a lesser extent, the finer-resolution grid (DX500) in Experiment B produces smaller temperature errors than the control case (C512), but larger errors in the low-level moisture field. In Experiment C, temperature errors are unexpectedly smaller in the simulation with fewest vertical grid levels (Z32), and nearly identical between the control and highest vertical-resolution case (Z50). In addition, the height of the maximum error in the low-level moisture field is related to the vertical resolution of the grid levels for Experiment C. This is because the maximum low-level moisture error for the simulations is related to the depth of the boundary layer used in the surface flux calculations. Even with the relatively large temperature and moisture errors in the four experiments, the temperature and moisture errors for the GCE model are on average smaller than the other models participating in the GCSS WG4 Case2 experiment (Krueger and Lazarus 1999). The cold temperature bias and low-level drying in the WG4 CRM and SCM results may be associated with errors in the sounding measurements as discussed by Zipser and Johnson (1998).

c. Evaluation of thermodynamics and dynamics in Experiment A.

In order to better understanding the causes of the large thermodynamic errors for Experiment A, we now examine more closely the simulated system thermodynamics, dynamics, cloud structure and precipitation fields.

1) Temperature and moisture perturbations

Figure 9 shows the root-mean-squared (rms) differences for the simulated temperature and moisture deviations for Experiment A. It is shown that although the largest domain produces smaller mean errors in temperature and moisture, the rms differences are greater for N1024 and smallest in N128. Thus fluctuations in the temperature and moisture perturbations increase with increasing domain size. This indicates that the larger grid (N1024) has greater fluctuations in at least some of the external forcings of radiational heating/cooling, cloud microphysical processes, surface fluxes, and cloud-scale updrafts and downdrafts. Peaks in the rms differences for moisture reaches a maximum of 1.2 g kg^{-1} near 950 mb, or near the top of the boundary layer and then decreases with altitude in the troposphere. Peak rms differences for temperature reach a maximum of 0.9 K at the surface for case N1024. In addition the differences between the rms deviations tends to increase in the lower troposphere. This shows that the mechanisms responsible for the temperature and moisture differences between the domains have a large influence within and near the top of the boundary layer likely due to air-sea interactions, but also extend throughout the troposphere. The next sections will examine these mechanisms in more detail.

2) CLOUDINESS

Figure 10 shows the mean cloud fraction and cloud-water-ice mixing ratio for Experiment A. For this study, the cloud fraction is defined as:

$$\sigma = 1 \quad \text{if } q_c + q_i > 0.01q^*(\bar{T}, \bar{p}), \quad \text{otherwise } \sigma = 0 \quad (4)$$

where q_c and q_i are the cloud water and cloud ice mixing ratios respectively, and q^* is the saturated mixing ratio over water. Experiment A has more variation in the cloud fraction than do the other three experiments (not shown). Cloudiness for this case is found to be inversely related to the domain grid size, with case N128 having the greatest mean cloud fraction in the cloud water and ice regions, and N1024 the lowest. The cloud fraction differences are larger in the cloud water regions (500-900mb), where case N128 reaches 20% and case N1024

cloudiness and cloud water mass only attains about half those levels. Cloudiness differences are smaller in the cloud-ice regions above 400 mb, where cloud fractions reach 82% in N128, and 77% for N1024. Only small differences exist between the other hydrometeor fields of rain, snow, and graupel (Fig. 11). It should be noted that although mean snow, representing anvil regions, is greater in the smallest domain (N128), graupel production, representing convective activity, is greater in the largest domain (N1024), suggesting stronger updrafts/downdrafts as the domain size increases. As discussed in the next section, cloud water is largely produced in convective updrafts, which is mainly triggered by unstable environments primarily responding to the large-scale advective temperature and moisture forcings. The overproduction of cloud water in simulation N128 indicates that the smaller domain cannot adequately respond to the large-scale forcings and corresponds to the fact that many tropical systems in the West-Pacific Ocean region tend to have scale sizes greater than 200 km. This overproduction of cloudiness in the smaller domain is what leads to the larger mid-level (600-800 mb) moisture deviations shown in Fig. 8a. However since case N128 produces on average 7.3 mm less rainfall (Table 3), it can be implied that greater evaporation and sublimation is occurring in the smaller grid, which is leading to greater net cooling (Fig. 7a). Further discussion of the net cooling and moistening effects of the smaller domain will be presented later.

3) RADIATION

One set of external forcings, which can change the mean simulated temperatures, is the shortwave and longwave radiational heating (Fig. 12). Due to the greater cloud cover in the smaller domain, case N128 has approximately 0.1 K day^{-1} less shortwave warming below the cloud water layer ($< 600 \text{ mb}$) than the N1024 case, but also about 0.5 K day^{-1} less longwave cooling, resulting in net warming near 0.4 K day^{-1} for case N128 relative to N1024. Radiational heating and cooling differences are smaller elsewhere except near the tropopause (200 mb) where longwave cooling rates above cloud top are greater in the N128 simulation compared to the N1024 case, due to greater cloud cover in the smaller domain. The radiational cooling above cloud tops (above 150 mb) is the dominant term in the overall

temperature deviations at these levels shown in Fig. 7. However, below the clouds, the net shortwave and longwave radiative heating/cooling rates results in less cooling for the smaller domain (N128) than in the larger (N1024), which is contrary to the mean temperature deviations below cloud tops shown in Fig. 7. Thus radiative heating/cooling is not a contributor to the mean temperature differences between the simulations.

4) SURFACE FLUXES

Heat and moisture fluxes emanating from the ocean represent additional external forcings to both the heat and moisture budgets, in the otherwise closed modeling system. Figure 13 and Table 4 shows the domain-averaged and mean sensible and latent heat fluxes from the ocean surface. The sensible heat fluxes generally range between 5 and 45 W m^{-2} , and the latent fluxes between 70 and 275 W m^{-2} , with fairly close agreement between the three simulations. There is a tendency for overestimation of the surface heat and moisture fluxes during times of increasing low-level wind speeds (Fig. 2) on 22 and 25 December, with greater relative differences from observed for the sensible heat fluxes. Grabowski et al. (1998) and Wu et al. (1998) have noted the same tendencies for the overproduction of sensible and to a lesser extent, latent heat fluxes for GATE and TOGA-COARE CRM simulations. Since observations fail to include enhancement of surface fluxes due to convection, the observed fluxes are likely too small since this was, in general, an active convective period. Table 4 shows that the mean sensible heat fluxes decrease slightly with increasing grid domain, from 25.1 W m^{-2} for case N128 to 22.8 W m^{-2} for case N1024. Conversely mean latent heat fluxes increase significantly with domain size from 148.0 W m^{-2} for case N128, to 172.1 W m^{-2} for case N1024. The increased mean latent heat flux with the larger domains is primarily a result of greater wind gusts from cold convective outflows. Greater wind gusts also increase sensible fluxes with the larger domain, but these are more than offset by the significantly cooler low-level air temperatures, (and hence larger vertical air-sea temperature gradients) in the smaller domain. The increased latent heat fluxes with domain size contributes to greater moisture in the boundary layer for N1024 as shown in Fig. 8a, but does not lead to greater cloudiness and moisture above the boundary layer, compared to case N128.

Hence additional processes, such as the dynamics or microphysics, are contributing to the mean thermodynamic differences.

5) DYNAMICS

Figure 14 shows the average peak upward and downward vertical velocities and mean cloud updraft and downdraft mass fluxes for experiment A. On average, maximum updrafts and downdrafts are greatest for the largest domain (N1024), and weakest for the smallest domain (N128). Average maximum upward vertical velocities are located in the 600 to 800 mb region and approach 5.8 m s^{-1} for case N1024 or nearly three times that of N128. This is located in the cloud water region, indicating that the larger domain has stronger convective updraft cores. Maximum downdrafts are also greatest in the cloud-layer between 600 and 800 mb where differences between the cases are less and maximum downdrafts are nearly twice as strong for case N1024 when compared to N128. The strongest vertical motions, as expected, are located in cloudy regions (Fig. 14b), while in clear regions, vertical motions are significantly weaker but largest for case N128. The vertical mass fluxes follow a similar pattern to the vertical velocities below 600 mb, except that the mass flux profiles for cases N512 and N1024 are nearly identical. Even so, the mean temperature and moisture deviations in cloudy regions (Figs. 15 and 16) show differences between C512 and N1024 which resemble the overall temperature differences shown in Figs. 7a and 8a. This implies that heating/cooling and evaporation/condensation due to downdrafts/updrafts is a rather small contributor to the overall mean temperature and moisture deviations between the simulations, and the deviations are primarily confined to cloudy regions.

6) RAINFALL

Overall the simulations did well in reproducing the observed five rainfall events in both duration and peak amount (Fig.17). The good correlation of simulated and total rainfall between the simulations and observations agrees with the high correlation of latent heating profiles between the simulations and observations (Fig. 4). This in turn is primarily a

response to the large-scale temperature and moisture advective forcings. However, as shown in Table 3, there is an increase in surface rainfall with domain size from 157.8 mm for N128, to 165.1 mm for N1024. Since more rainfall is reaching the surface as the domain size increases, less net evaporation is occurring in the N1024 case, leading to warmer low-level temperatures and reduced low-level moisture (near 900 mb) as shown in Figs. 7a and 8a. Note that the control case (C512) with 161.6 mm, matches very closely to the observed rainfall of 160.8 mm. Maximum rainfall rates generally agree well with observations, with some reduction on the 25 December event, when observed peak rates were 73 mm day^{-1} , and simulated values were near 60 mm day^{-1} .

The Hovmuller plots of surface rainfall rates for experiment A (Fig. 18) show both fast moving eastward ($\sim 8\text{-}12 \text{ m s}^{-1}$), and slower, westward-moving squall-line disturbances ($\sim 3\text{-}5 \text{ m s}^{-1}$) in the C512 and N1024 simulations. Except for the early period before 21 December, the smallest domain (N128) generally only shows the systems propagating to the ESE, while the two larger domains show larger westward propagating systems with heavy rainfall. Observations during this period did confirm both the easterly and westerly propagating events (Chen et al. 1996) which are organized by the larger-scale vertical wind shear. This again provides evidence that domain size of at least 500 km is necessary to resolve the convective features of tropical systems in the West Pacific since more physical space is required for the clouds to develop into larger mesoscale structures.

7) INTEGRATED TOTALS

To better ascertain the causes for the thermodynamic differences between the domain dependent simulations, an examination of the contributions to the temperature and water vapor equations is now made. Integrating the equations for temperature (T) and water vapor (q_v) over the horizontal and from the surface to the top of the model domain yields:

$$\left\langle \frac{\partial \bar{p} \bar{T}}{\partial t} \right\rangle = \left\langle \frac{L_v}{C_p} \bar{p} (\bar{c} - \bar{e}) + \frac{L_s}{C_p} \bar{p} (\bar{d} - \bar{s}) + \bar{p} \frac{L_f}{C_p} (\bar{f} - \bar{m}) \right\rangle - \left\langle \bar{w} \frac{\partial \bar{p} \bar{T}}{\partial z} \right\rangle + \frac{1}{C_p} \langle Q_R \rangle + \bar{H}_s \quad (5)$$

$$L_v < \frac{\partial \bar{\rho} \bar{q}_v}{\partial t} > = - < L_v \bar{\rho} (\bar{c} - \bar{e}) + L_s \bar{\rho} (\bar{d} - \bar{s}) > - L_v < \bar{w} \frac{\partial \bar{\rho} \bar{q}_v}{\partial z} > + L_v \bar{E}_o \quad (6)$$

where c , e , d , s , f , and m are condensation, evaporation, deposition, sublimation, freezing, and melting of cloud, respectively. The second terms to the right in (5) and (6) are the imposed large-scale advective temperature and moisture forcings, Q_R is net radiational heating or cooling, and H_s and E_o are the sensible and latent heat fluxes from the ocean surface.

Tables 5 and 6 list the individual components of the temperature and water vapor budgets for experiment A from eqs. (5) and (6) respectively. Table 5 shows that the largest domain (N1024) has an integrated average temperature that is 1.11 K warmer than the smallest domain (N128), which agrees well with the mean temperature deviations shown in Fig. 7a. Since the large-scale forcing is prescribed (term C), the temperature differences must arise from terms B, D, and E in table 5, namely microphysical processes, radiation, and surface sensible heat fluxes. As discussed earlier and shown in Figs. 12, 13, and Table 4, both the radiation and surface sensible heat flux contribute to a negative difference between N1024 and N128, the former leading to a net cooling of 0.72 K, and the later to 0.19 K net cooling. Therefore the cause of the warmer domain for N1024 is due to relatively greater latent heating resulting from microphysical processes. Although this first appears to contradict the greater condensation and cloud water found in N128 (Fig. 10), a more detailed analysis reveals that evaporation is even greater in N128, thus leading to larger net condensation and warming for N1024. Table 5 also shows that microphysical processes are the primary response to the large-scale forcing, while sensible heat fluxes and radiation combined are more than an order of magnitude smaller.

Table 6 shows the unlike the temperature components, surface fluxes, namely the release of latent heat from the ocean surface, plays a much more important role in the overall water budgets. Latent heat fluxes have a magnitude approximately 1/3 of the total large-scale advective moisture forcing, and microphysical processes respond to the combination of both the large-scale advective and surface latent fluxes. As discussed earlier and shown in Fig. 13 and Table 4, case N1024 produces significantly greater latent heat fluxes than N128, resulting

in a net mean column integrated water amount which is 6.14 mm greater than N128. However the greater net condensation in N1024 (due to less evaporation) compared to N128, results in 7.78 mm less integrated water in the larger domain. The result is a net difference of -1.63 mm, or approximately 0.5 g kg^{-1} over the lowest 6 km of the domain, again agreeing well with the mean moisture deviations shown in Fig. 8a. Therefore both microphysical and surface fluxes play significant roles in explaining the overall net differences of the mean moisture deviations in experiment A.

5. Results from the control experiment

In order to better understand the physical processes involved with deep convection and the relation of the simulated events with the large-scale environment, a more detailed examination is now given of the thermodynamic, dynamic, and microphysical processes for the control case, C512.

a. Q1, Q2 budgets and cloud fields

1) Q1 and Q2 total budgets

The vertical distributions of convective latent heat release, and moisture in the tropics leads to modulations of the large-scale tropical circulations, and in turn, the energy budgets on a global scale. In order to quantify this energy release in diagnostic (*e.g.*, Yanai *et al.*, 1973) and modeling studies, it is customary to define the apparent heat source Q_1 , and the apparent moisture sink Q_2 of a large-scale system by averaging horizontally the thermodynamic equation (θ , potential temperature) as:

$$Q_1 = \bar{\pi} \left(\frac{\partial \bar{\theta}}{\partial t} + \bar{\mathbf{V}} \cdot \nabla \bar{\theta} + \bar{w} \frac{\partial \bar{\theta}}{\partial z} \right) \quad (7)$$

$$Q_2 = -\frac{L_v}{C_p} \left[\frac{\partial \bar{q}_v}{\partial t} + \bar{\mathbf{V}} \cdot \nabla \bar{q}_v + \bar{w} \frac{\partial \bar{q}_v}{\partial z} \right] \quad (8)$$

Q_1 and Q_2 can be calculated either from observations or from grid values in a large- or regional-scale prediction model. Q_1 and Q_2 can be directly related to the contributions of cloud effects, which can be explicitly estimated by the GCE model (Soong and Tao, 1980; Tao, 1983; Tao and Soong, 1986; Tao and Simpson, 1989b):

$$Q_1 = \bar{\pi} \left[-\frac{1}{\bar{\rho}} \frac{\partial \bar{\rho} w' \theta'}{\partial z} + D_\theta \right] + \frac{L_v}{C_p} (\bar{c} - \bar{e}_c - \bar{e}_r) + \frac{L_f}{C_p} (\bar{f} - \bar{m}) + \frac{L_s}{C_p} (\bar{d} - \bar{s}) + \bar{Q}_R \quad (9)$$

$$Q_2 = \frac{L_v}{C_p} \left[\frac{1}{\bar{\rho}} \frac{\partial \bar{\rho} w' q'_v}{\partial z} - \bar{D}_{qv} \right] + \frac{L_v}{C_p} (\bar{c} - \bar{e}_c - \bar{e}_r) + \frac{L_s}{C_p} (\bar{d} - \bar{s}) \quad (10)$$

The overbars denote horizontal averages, and the primes indicate deviations from the horizontal averages. The variable $\bar{\rho}$ is the air density, and $\bar{\pi} = \left(\frac{p}{P_0} \right)^{\frac{R}{C_p}}$ is the nondimensional pressure, where p is the dimensional pressure and P_0 the reference pressure taken to be 1000 mb. The first terms on the right-hand sides of (9) and (10) are the vertical eddy heat and moisture flux convergences. The subgrid-scale turbulence terms are represented by D_θ and D_q and are negligible compared to other terms above the boundary layer (Soong and Tao, 1980; Krueger, 1988). The other symbols are defined in eqs. (5) and (6). Overall, eqns. (9) and (10) represent the atmospheric heating and drying effects, respectively, of the cloud systems.

Figure 19 shows the C512 simulated and TOGA-COARE IFA diagnosed (Lin and Johnson, 1996) Q_1 and Q_2 fields for the entire 8-day period. Overall the model does well in simulating the heating and drying effects of the atmosphere for the five major convective events, with Q_1 and Q_2 peaks each reaching 30 to 40 K day⁻¹. This can be attributed to the primary response of the atmospheric system to the large-scale advective forcings shown in

Fig. 3 and Tables 5 and 6. At times the simulated Q1 and Q2 fields have weaker magnitudes than diagnosed, most notably on 22 December. Although the cause of these differences are uncertain, deviations between the simulated and observed atmospheric water vapor mixing ratio were much greater during this period, which we suspect were largely related to erroneous moisture errors in the soundings. In general, there is also more small-scale structure in the simulated Q1 and Q2 fields, which can be attributed to cloud- and subgrid-scale nonlinear effects, filtering, and averaging. There is also greater structure in the low-level Q2 fields, with significant moistening of up to 20 K day^{-1} occurring below 900 mb after the major convective events. This moistening is primarily due to latent heat fluxes from the ocean surface (a major contributor to the water vapor budget shown in Table 6) being confined to the boundary layer in relatively stable air masses. Finally it should be noted that the major convective events of 20, 21, 22, and 24 December all preceded increasing low to mid-level westerly winds, and increasing atmospheric shear as shown in Fig. 2a.

2) Q1, Q2 components

In order to better understand the major contributions to the atmospheric heating/cooling and drying/moistening, the individual components of the mean Q1 and Q2 budgets for case C512 are computed and shown in Fig. 20 and 21. For Q1 (Fig. 20), the dominant terms are the microphysical conversion rates for condensation/evaporation below 300 mb, and deposition/sublimation of ice between 200 and 500 mb. The secondary heating terms, which include melting, freezing, shortwave and longwave radiation, and turbulent transfer, have absolute heating rates generally less than 1 K day^{-1} (Fig. 20b), except for at the melting layer near 600 mb. Near the surface, the turbulent transfer contributes about 2 K day^{-1} heating which is mainly offset by evaporative cooling of rainwater, leading to negligible heating rates below 950 mb as shown in Fig. 19a. Between 950 and 700 mb, heating due to condensation increases to 9 K day^{-1} , while evaporative cooling remains near 4 K day^{-1} , which contributes to increased latent heating to 5 K day^{-1} in this region (see Fig. 4). At the melting level near 600 mb, condensational heating reaches a peak of 11 K day^{-1} , melting contributes 3 K day^{-1} cooling, as does evaporation. The combination of turbulent transfer, freezing, and deposition

just above the melting layer adds an additional 3 K day^{-1} leading to a total 8 K day^{-1} heating rate. From 550 to 450 mb, total latent heating increases rapidly, primarily due to the additional latent energy from the deposition of water vapor to ice. Further aloft at 350 mb, deposition and sublimation rates reach maximum values with deposition heating rates of 23 K day^{-1} slightly exceeding sublimation rates of 20 K day^{-1} . This, along with the fact that the deposition of ice exists over a much deeper layer than sublimation (400 vs. 200 mb respectively), again contributes to the positive heating curves shown in Fig. 4a.

There are fewer terms for the Q2 budget (Fig. 21), with condensation, evaporation, deposition, and sublimation comprising the major terms. Mean condensation exceeds evaporation throughout the troposphere, which leads to an overall net atmospheric drying which peaks near 5 g kg^{-1} in the cloud layer at approximately 600 mb (Fig. 10a). In the same manner, mean deposition exceeds sublimation, leading to a net atmospheric drying of approximately 1 g kg^{-1} near 350 mb in the cloud ice region. Diffusion is found to play a larger role in Q2 than in Q1. Except in the lowest 50 mb, where diffusion leads to 0.6 g kg^{-1} moistening due to surface latent fluxes, turbulent transfer leads to overall drying of the atmosphere. Peak drying from turbulent processes reaches a maximum of 1.5 g kg^{-1} (equivalent to 4 K Day^{-1}) near 600 mb, where ambient air is being entrained into the clouds.

Overall, except near the surface, it is shown that in response to the large-scale forcings, microphysical processes play a primary role in the overall Q1 and Q2 budgets in the atmosphere, while turbulent transfer and radiation play smaller roles. This agrees with the integrated heating and moistening values for experiment A (Tables 5 and 6). In addition, condensational warming and drying exceeds evaporation throughout the atmosphere, except in the lowest 30-40 mb near the surface, where evaporative cooling and moistening dominates. Higher aloft above 400 mb, deposition and sublimation dominate, with overall deposition rates exceeding sublimation, leading to a net atmospheric warming and drying.

3) Convective-stratiform separation

The GCE convective-stratiform partitioning scheme (CSPS) was applied in this study to the control case (C512) in order to identify the role in which convective and stratiform

regimes play in budgets, fluxes, rainfall, and cloud fields during active events. Knowledge of these features can then be applied to better understand the structure of tropical systems, and for improved precipitation and latent heating retrievals in conjunction with remote sensing measurements from instruments including TRMM and SSM/I. In the CSPS, convective, stratiform, and non-surface precipitation regions are first identified using the information from surface rain rates (Churchill and Houze, 1984). Two additional criteria are then applied to identify regions where convection is active aloft, although little or no precipitation exists at the surface. This could include regions with tilted updrafts and convective cellular initiation ahead of organized squall lines (Tao et al., 1993). The determining factor when non-surface precipitation regions are considered to be convective, is when cloud water exceeds a defined threshold (i.e., the minimum of either $q_c = 0.5 \text{ g kg}^{-1}$, or $\frac{1}{2} q_{c\text{max}}$ at that specific time), or if the updraft exceeds a certain threshold (i.e., the minimum value between 3 m s^{-1} and $\frac{1}{2}$ the maximum updraft at that specific time) below the melting level. For the region classified as stratiform, additional criteria are considered to identify active convective cells aloft. The first one is to check the updraft velocity above the melting level. The second one is to check cloud water and cloud ice content beneath the melting level (Tao and Simpson, 1989b; and Tao et al., 1993). The threshold values may need to be adjusted for different cloud systems as well as various stages of their life cycle.

Figure 22 shows that there are very distinct differences between the simulated convective and stratiform Q1 and Q2 domain-averaged fields, which are separated using the CSPS. The atmospheric heating and drying associated with the convective events is located primarily in cloud updraft regions and is thus highly correlated with regions of cloud water condensation below 500 mb (Fig. 23c) and large graupel production between 600 and 300 mb (Fig. 23a). Graupel production is related to the intensity of the cloud updraft, with the largest graupel mixing ratios exceeding 1 g kg^{-1} on 24-25 December. Note that there is a lack of graupel production on 22 December, which is resulting in reduced simulated Q1 values in comparison to observations. Again we theorize that this is largely due to errors in the moisture sounding measurements. Overall, the convective regions are producing maximum heating and drying rates exceeding 35 and 45 K Day^{-1} respectively during the 24-25 December event. For the stratiform regions, the atmospheric heating and drying is located above the

melting level near 600 mb, in regions of snow and ice deposition (Fig. 23b). Here the values of Q2 are, in particular, weaker than the convective regions due to reduced water vapor and deposition rates of the lower density ice particles. Below 600 mb in the stratiform regions, cooling and strong moistening exists due to the evaporation of rainwater produced largely from the melting of graupel (Fig. 23d). Stratiform cooling rates are typically between 5 and 10 K day⁻¹, while low-level stratiform moistening rates at times exceed 35 K day⁻¹ between 800 and 900 mb. Note that convective warming and drying are occurring at the same levels as the stratiform low-level cooling and moistening, indicating the contrasting thermodynamical characteristics for the two regimes.

b. Vertical mass fluxes

Figure 24 shows mean and domain-averaged fields of the total, convective, and stratiform vertical mass fluxes for case C512. The total mass flux shows five distinct maxima which correspond to the five precipitating events shown in the Q1 and Q2 profiles (Fig. 19). During the largest event on 24 December, the domain-averaged total flux reaches values exceeding 0.06 kg m⁻² s⁻¹ near 450 mb. Other peak updraft mass fluxes are located between 400 and 550 mb, and are highly dependent on the amount and location of ice particles in stratiform regions, and thus the depositional growth of ice providing additional latent heat aloft. For example, the total domain-averaged mass flux on the 22 December case is 0.055 kg m⁻² s⁻¹ at 400 mb. This case also has greater stratiform snow amounts (Fig. 23b) and greater stratiform upward mass fluxes than the other events. Figure 24b shows that above the melting layer near 500 mb, upward mass fluxes in stratiform regions exceed those in convective regions. The combination of the stratiform and convective components of the mass fluxes produces a peak upward mean total mass flux of 0.02 kg m⁻² s⁻¹ at 450 mb. Below 600 mb, evaporative cooling and moistening of the atmosphere, from rainfall primarily produced by the melting of graupel, is leading to a peak mean downward mass flux within stratiform regions of -0.015 kg m⁻² s⁻¹ at 775 mb. Total net downward mass flux reaches a maximum near the end of major events (Fig. 24a) when systems are in their final stages. Maximum updraft mass fluxes occur in convective regions near 725 mb and are fueled by latent heat

release of condensation in the production of cloud water. The peak convective updraft mass flux is therefore located at approximately the same heights and times as the peak downward mass flux in the stratiform regions. This indicates the strong cellular nature of the low-level vertical velocity fields, and the contrasting dynamical characteristics which exist between the convective and stratiform regions.

c. Hydrometeor fields

Since heat and moisture release through microphysical conversions are shown to be the primary response to the large-scale atmospheric forcings, an examination of the microphysical features of a convective event is now presented in order to better understand these processes. Figure 25 shows cross-sectional contour plots of each hydrometeor mass species during an active precipitating period for this study (23 UTC 24 December). A noticeable feature of this system is the relatively narrow and vertically oriented bands of strong updrafts shown by the cloud water fields in Fig. 25a. These updraft bands are typically 5 to 10 km in diameter, have maximum cloud water mixing ratios exceeding 1.0 g kg^{-1} , and extend from near the surface to approximately 300 mb. The vertical structure of these bands indicates that they are short-lived, with cells forming and dying on a scale of 1 to 2 hours. The remnants of past convective cells are evident by the stratified layers of cloud ice, snow, graupel, and rain, which extend up to several hundred km away from the updraft cores. The elevation of these layers is inversely related to the density of the hydrometeor species, with cloud ice (Fig. 25b) located above 350 mb, cloud snow (Fig. 25d) above 600 mb (melting layer), graupel (Fig. 25e) above 650 mb, and rain (Fig. 25c) below the melting layer near 600 mb. Thus as cloud ice aggregates it falls as snow, which rimes by cloud water to form graupel, and then melts to produce rainwater. It should be noted that these are the primary mechanisms, but many secondary processes exist as well. Graupel mixing ratios exceed 1.0 g kg^{-1} near and in the updraft cores between NX=128 and 256, and the graupel mass is primarily created by the riming of snow and ice by the greater cloud water mass in these regions, and the larger vertical velocities which allow graupel particles to remain aloft. Rainwater produced from the melting of graupel in these regions is classified as 'convective', while rain in other regions is classified as 'stratiform'. Note that much of the rainwater in the stratiform regions is evaporating before

reaching the surface between $X=0$ and 100, and $X=270$ and 512. Snow aggregates, during this period, extend throughout the domain between 100 and 600 mb and have mixing ratios exceeding 0.1 g kg^{-1} in the convective regions between 350 and 500 mb. The large anvil demonstrates the extensive size of this convective event, and also the impact that cyclical boundary conditions have on the sublimation and conversions of ice particles to other species or vapor.

d. Rainfall

Figure 26 shows that the simulated domain-averaged total rainfall matches reasonably well with the IFA observed rainfall, with maximum differences of approximately 10 mm day^{-1} occurring on 24 December. The overall mean total surface rainfall between the simulation and observed IFA region (Table 7) differed by only 0.3 mm, which testifies to the accurate reproduction of the latent heating fields (Fig 19) in the simulation, which again was primarily a response from the imposed large-scale advection of temperature and moisture. Table 7 shows that 86.1mm or 53.3% of the total simulated rainfall is classified as convective using the CSPS, while 75.5 mm or 46.7% is classified as stratiform. Thus both convective and stratiform rainfall constitutes nearly 1/2 of the total rain. The slightly greater proportion of convective rainfall is consistent with other tropical rainfall events given in Tao et al. (1997, 2000. Figure 26 shows that for approximately 2/3 of the time, convective rainfall rates exceed stratiform rates by 1 to 8 mm day^{-1} , with stratiform rates exceeding convective on 22 and 25 December. The former period is associated with the greater simulated stratiform snow (Fig. 23b) amounts, and the later is during the demise (anvil remnant) of the large convective episode of 24 December.

The Hovmueller diagrams shown in Fig. 27 show that stratiform rainfall covers approximately 90% of the total surface rainfall area, but the convective rain rates are over ten times as strong as the stratiform rates. Both the stratiform and convective rainfall patterns closely resemble the coverage of the total rainfall given in Fig. 18, with both the fast moving eastward, and slower, westward-moving squall-line disturbances, most notably on 24 and 25 December. The lower rain rates in the stratiform region are due to smaller raindrops reaching

the surface compared to convective rainfall, and greater evaporation below the stratiform cloud deck. Droplets in the stratiform region are primarily being formed from the melting of small graupel and snow aggregates falling below the melting layer, while the larger rainwater drops in the convective region develop mainly from the melting of larger graupel particles, which form and grow in and near the stronger updraft cores.

e. Surface fluxes

Figure 28 shows the domain-averaged sensible and latent heat fluxes for both the control simulation (C512) and the observed TOGA-COARE flux taken from the IMET buoy. In an attempt to understand the cause(s) of why the simulated fluxes exceed the observed values shown in Table 4, the mean surface wind speed and wind speed standard deviation are also included. As expected both the latent and sensible heat fluxes closely follow the mean surface-wind speed pattern, and for the first two days closely match the corresponding observed heat fluxes. After 21 December, and on 26 December, mean wind speeds increase to $> 5 \text{ m s}^{-1}$ and both the latent and sensible heat fluxes exceed their respective observed values. This is not the case when mean wind speeds increase during 25 December. The wind speed standard deviation does show a decrease to less than 2 m s^{-1} on late 25 December which would indicate that wind gustiness is less during this period and could be a factor for the better agreement. It should be noted, however, that the sensible heat flux is too large on 23-24 December while latent fluxes remain close to observations during the same period. Therefore the cause of the larger than observed heat fluxes appears to be twofold: (a) over prediction by the aerodynamic surface flux formulation when surface wind speeds become large, and (b) the computation of the observed fluxes from a single point within the IFA from the IMET buoy. Thus for (b) the surface air temperature, moisture, and SST and their deviations, are less representative of the entire IFA compared to the domain-averaged simulated fluxes.

6. Summary and Conclusions

In this study, the 2-D GCE model utilized periodic boundary conditions, and included large-scale diagnosed thermodynamic and momentum advective forcings to simulate, semi-prognostically, the active convective period of 19-27 December 1992 over the TOGA-COARE IFA. From the four initial experiments conducted in this study, it was found that grid domain size played a more significant role on the mean temperature and moisture errors than did both horizontal and vertical grid resolution, and vertical filtering. The type of vertical filtering algorithm incorporated did play an important role in the distribution of hydrometeor species, especially ice, with the positive definite scheme producing smoother and more realistic cloud fields. The smallest mean temperature and moisture errors, and most accurate representation of the cloud system in terms of cloud water and ice fractions occurred with the largest grid (N1024), and to a lesser extent, the finer resolution (DX500) simulations. It was shown that a horizontal domain of at least 512 km was needed to resolve the active convective cloud-system features, which had scales of several hundred km. The smaller grid (N128) allowed more cloud water and ice mass to remain in the model domain, leading to a greater, and more unrealistic, layer of cloudiness near the 200-mb ice- and 600-mb cloud water-layer regions. The smaller temperature errors in case N1024 relative to N128 was found to be caused by greater latent heating release due to more net condensation and deposition in the largest domain. The greater latent heat release in N1024 was caused by larger vertical motions, in particular updrafts and compensating downdrafts, which was the result of a drier and more unstable mid-level atmosphere in the larger domain. Greater net condensation for N1024 also produced a drier atmosphere in the largest domain, which was largely offset for this case by greater surface latent heat fluxes. Overall the increased latent heat release with increasing grid domain size resulted in 7.3 mm more total rainfall for case N1024 compared to case N128.

In the control simulation, the Q1 and Q2 fields closely resembled the diagnosed values throughout the troposphere, indicating the primary response of the atmospheric system to the large-scale forcings of temperature, moisture, and horizontal momentum advection. Greater differences were noted in the boundary layer due to surface fluxes and low-level vertical transport of heat and moisture. An examination of the individual components, which comprise the Q1 and Q2 budgets, showed that the physical processes of condensation/evaporation and deposition/sublimation were the primary responses to the large-scale atmospheric forcings, except for near the surface, where diffusion processes were similar in magnitude to evaporation. Melting in the Q1 budget and

turbulent transport in the Q2 budget were also significant processes near the melting level at 600 mb, while radiation played only a minor role in the overall Q1 budget. Since rainfall can be estimated from the vertical distributions of convective latent heat release, GCE-simulated heating profiles such as these are being used to develop heating retrieval and rainfall algorithms for the Tropical Rainfall Measuring Mission (TRMM). Accurate rainfall measurements in the tropics are important since rainfall is a key link in the hydrologic cycle, as well as the primary heat source for the atmosphere.

A breakdown of the total heating and moistening budgets into convective and stratiform regimes showed that convective heating and drying was located in cloud updraft regions where cloud water and larger graupel were predominant. Conversely, stratiform heating and drying was confined to regions above the melting layer (600 mb) in regions of ice and snow deposition, while stratiform cooling and moistening was located below 600 mb in regions of evaporating rain. Overall atmospheric heating was found to be greatest in the updraft cores near 600 mb, while atmospheric moistening was found to be largest in the evaporating rainwater downdrafts near 800 mb. This results in upward mass fluxes in convective and downward mass fluxes in stratiform regions between 600 mb and the surface, with peak downward fluxes occurring near the end of the convective system life. Rainfall rates were much greater in convective regions, but since stratiform regions covered approximately 90% of the total domain, the total convective rainfall was only slightly greater than the total stratiform rainfall.

The ensemble of systems simulated included both the fast moving eastward, and slower, westward-moving squall-line disturbances. Updraft regions containing cloud water typically ranged between 5 and 10 km in diameter, while large anvils of snow, ice, and graupel covered the entire domain during the more active periods. Cyclical boundaries contributed to greater moisture in the midlevels for the smaller domains. In addition, the storm was shown to be unresolved on the smallest domain of 128 km and minimally resolved on C512. Thus future deep tropical simulations should consider larger horizontal domains of 1000 km or more, for long-term integrations using large-scale forcings and cyclical boundaries.

There were, at times, significant differences between the observed and simulated sensible and latent heat fluxes. Surface fluxes were near those observed for much of the quiescent periods, but were greater than observed during periods with higher wind gusts. Reasons for the surface flux

errors are likely due to the overprediction by the aerodynamic surface flux formulation, and the computation of the observed fluxes from a single point, the IMET buoy.

As a final note, the GCE model results for this simulation have, overall, compared very favorably to the results of seven other cloud-resolving models which participated in the GCSS WG4 Case2 study. Temperature, moisture, and total radiative heating errors for the GCE models were among the smallest of all the models. The GCE did produce less cloud water and ice than did the other models, which may be partly attributed to the microphysical parameterization scheme in the GCE. The GCE model also produced greater shortwave heating rates near the surface, and smaller shortwave heating rates in the upper atmosphere, which can be attributed to smaller cloud amounts and the method used to compute the hydrometeor effective radius. More information about this study and the results from the model participants can be found in Krueger and Lazarus (1999).

Acknowledgements. We thank Drs. Lin and R. Johnson for providing us with their calculations of heating profiles and large-scale forcing for the GCE model simulations and validations.

The Goddard Cumulus Ensemble Model group is supported by the NASA Headquarters Physical Climate Program and by the NASA TRMM project. The authors are grateful to Dr. R. Kakar (NASA/HQ) for his support of this research. Acknowledgment is also made to NASA/Goddard Space Flight Center for computer time used in the research.

7. References

- Chen, S. S., R. A. Houze, and B. E. Mapes, 1996: Multiscale variability of deep convection in relation to large-scale circulation in TOGA COARE, *J. Atmos. Sci.*, **53**, 1380-1409.
- Chou, M.-D., 1984: Broadband water vapor transmission functions for atmospheric IR flux computation. *J. Atmos. Sci.*, **41**, 1775-1778.
- Chou, M.-D., 1986: Atmospheric solar heating rate in the water vapor bands. *J. Climate Appl. Meteor.*, **25**, 1532-1542.
- Chou, M.-D., 1990: Parameterization for the absorption of solar radiation by O₂ and CO₂ with application to climate studies. *J. Climate*, **3**, 209-217.
- Chou, M.-D., 1992: A solar radiation model for use in climate studies. *J. Atmos. Sci.*, **49**, 762-772.
- Churchill, D. D., and R. A. Houze, Jr., 1984: Development and structure of winter monsoon cloud clusters on 10 December 1978. *J. Atmos. Sci.*, **41**, 933-960.
- Donner, L. J., C. J. Seman and R. S. Hemler, 1999: Three-dimensional cloud-system modeling of GATE convection, *J. Atmos. Sci.*, **56**, 1885-1912.
- Dudhia, J., M. W. Moncrieff and D. W. K. So, 1987: Numerical simulation of quasi-stationary tropical convective bands. *Quart. J. Roy. Meteor. Soc.*, **113**, 929-967.
- Ferrier, B. S., 1994: A double-moment multiple-phase four-class bulk ice scheme. Part I: Description. *J. Atmos. Sci.*, **51**, 249-280.
- Ferrier, B. S., W.-K. Tao, and J. Simpson, 1995: A double-moment multiple-phase four-class bulk ice scheme. Part II: Simulations of convective storms in different large-scale environments and comparisons with other bulk parameterizations. *J. Atmos. Sci.*, **52**, 1001-1033.
- GCSS Science Team, 1993: The GEWEX Cloud System Study. *Bull. Amer. Meteor. Soc.*, **74**, 387-400.
- Grabowski, W. W., X. Wu, and M. W. Moncrieff, 1996: Cloud resolving modeling of tropical cloud systems during PHASE III of GATE. Part I: Two-dimensional experiments. *J. Atmos. Sci.*, **53**, 3684-3709.
- Grabowski, W. W., X. Wu, and M. W. Moncrieff, 1999: Cloud resolving modeling of tropical

- cloud systems during PHASE III of GATE. Part III: Effects of cloud microphysics. *J. Atmos. Sci.*, **56**, 2384-2402.
- Grabowski, W. W., X. Wu, M. W. Moncrieff, and W. D. Hall, 1998: Cloud resolving modeling of tropical cloud systems during PHASE III of GATE. Part II: Effects of resolution and the third dimension. *J. Atmos. Sci.*, **55**, 3264-3282.
- Held, I. M., R. S. Hemler, and V. Ramaswamy, 1993: Radiative-convective equilibrium with explicit two-dimensional moist convection. *J. Atmos. Sci.*, **50**, 3909-3927.
- Johnson, D., W.-K. Tao, J. Simpson, and C.-H. Sui, 2001: A Study of the Response of Deep Tropical Clouds to Large-Scale Processes, Part II sensitivities to microphysics, radiation, and surface fluxes, *J. Atmos. Sci.*, (submitted).
- Klemp, J. B., and R. Wilhelmson, 1978: The simulation of three-dimensional convective storm dynamics. *J. Atmos. Sci.*, **35**, 1070-1096.
- Krueger, S. K., 1988: Numerical simulation of tropical cumulus clouds and their interaction with the subcloud layer. *J. Atmos. Sci.*, **45**, 2221-2250.
- Krueger, S. K., and S. M. Lazarus, 1999: Intercomparison of multi-day simulations of convection during TOGA COARE with several cloud-resolving and single-column models. *Preprints, 23rd Conference on Hurricanes and Tropical Meteorology*, Dallas, TX, Amer. Meteor. Soc.
- Li, X., C.-H. Sui, K.-M. Lau and M.-D. Chou, 1999: Large-scale forcing and cloud-radiation interaction in the tropical deep convective regime. *J. Atmos. Sci.*, **56**, 3028-3042.
- Lin, Y.-L., R. D. Farley, and H. D. Orville, 1983: Bulk parameterization of the snow field in a cloud model. *J. Climate Appl. Meteor.*, **22**, 1065-1092.
- Lin, X., and R. H. Johnson, 1996: Heating, moistening and rainfall over the western Pacific during TOGA COARE. *J. Atmos. Sci.*, **53**, 3367-3383.
- Lipps, F. B., and R. S. Helmer, 1986: Numerical simulation of deep tropical convection associated with large-scale convergence. *J. Atmos. Sci.*, **43**, 1796-1816.
- Lynn, B. H., W.-K. Tao and P. Wetzel, 1998: A study of landscape generated deep moist convection, *Mon. Wea. Rev.*, **126**, 928-942.
- McCumber, M., W.-K. Tao, J. Simpson, R. Penc, and S.-T. Soong, 1991: Comparison of ice-phase microphysical parameterization schemes using numerical simulations of convection. *J. Appl. Meteor.*, **30**, 985-1004.

- Moncrieff, M. W., Steven K. Krueger, D. Gregory, J.-L. Redelsperger, and W.-K. Tao, 1997: GEWEX Cloud System Study (GCSS) Working Group 4: Precipitating convective cloud systems. *Bull Amer. Meteor. Soc.*, **78**, 831-845.
- Nakajima, K., and T. Matsuno, 1988: Numerical experiments concerning the origin of cloud cluster in tropical atmosphere. *J. Meteor. Soc. Japan*, **66**, 309-329.
- Ogrua, Y., and J.-Y. Jiang, 1985: A modeling study of heating and drying effects of convective clouds in an extratropical mesoscale system. *J. Atmos. Sci.*, **42**, 2478-2492.
- Rutledge, S.A., and P.V. Hobbs, 1984: The mesoscale and microscale structure and organization of clouds and precipitation in mid-latitude clouds. Part XII: A diagnostic modeling study of precipitation development in narrow cold frontal rainbands. *J. Atmos. Sci.*, **41**, 2949-2972.
- Simpson, J., and W.-K. Tao, 1993: The Goddard Cumulus Ensemble Model. Part II: Applications for studying cloud precipitating processes and for NASA TRMM. *Terrestrial, Atmospheric and Oceanic Sciences*, **4**, 73-116.
- Smolarkiewicz, P. K., 1983: A simple positive definite advection scheme with small implicit diffusion. *Mon. Wea. Rev.*, **111**, 479-486.
- Smolarkiewicz, P. K., 1984: a fully multidimensional positive definite advection transport algorithm with small implicit diffusion. *J. Comput. Phys.*, **54**, 325-362.
- Smolarkiewicz, P. K., and W. W. Grabowski, 1990: The multidimensional positive advection transport algorithm: Nonoscillatory option. *J. Comput. Phys.*, **86**, 355-375.
- Soong, S.-T., and Y. Ogura, 1980: Response of trade wind cumuli to large-scale processes. *J. Atmos. Sci.*, **37**, 2035-2050.
- Soong, S.-T., and W.-K. Tao, 1980: Response of deep tropical clouds to mesoscale processes. *J. Atmos. Sci.*, **37**, 2016-2036.
- Soong, S.-T., and W.-K. Tao, 1984: A numerical study of the vertical transport of momentum in a tropical rainband. *J. Atmos. Sci.*, **41**, 1049-1061.
- Su, H., S. S. Chen, and C. S. Bretherton, 1999: Three-dimensional week-long simulations of TOGA-COARE convective systems using the MM5 mesoscale model. *J. Atmos. Sci.*, **56**, 2326-2344.
- Sui, C. H., K. M. Lau, W.-K. Tao, and J. Simpson, 1994: The tropical water and energy cycles

- in a cumulus ensemble model. Part I: Equilibrium climate. *J. Atmos. Sci.*, **51**, 711-728.
- Tao, W.-K., 1983: A numerical study of the structure and vertical transport properties of a tropical convective system. Ph.D. Dissertation, Department of Atmospheric Science, University of Illinois, 228 pp.
- Tao, W.-K., and S.-T. Soong, 1986: A study of the response of deep tropical clouds to mesoscale processes: Three-dimensional numerical experiments. *J. Atmos. Sci.*, **43**, 2653-2676.
- Tao, W.-K., J. Simpson, and S.-T. Soong, 1987: Statistical properties of a cloud ensemble: A numerical study. *J. Atmos. Sci.*, **44**, 3175-3187.
- Tao, W.-K., and J. Simpson, 1989a: A further study of cumulus interaction and mergers: Three-dimensional simulations with trajectory analyses. *J. Atmos. Sci.*, **46**, 2974-3004.
- Tao, W.-K., and J. Simpson, 1989b: Modeling study of a tropical squall-type convective line. *J. Atmos. Sci.*, **46**, 177-202.
- Tao, W.-K., and J. Simpson, 1993: The Goddard Cumulus Ensemble Model. Part I: Model description. *Terrestrial, Atmospheric and Oceanic Sciences*, **4**, 19-54.
- Tao, W.-K., J. Simpson, C.-H. Sui, B. Ferrier, S. Lang, J. Scala, M.-D. Chou, and K. Pickering, 1993: Heating, moisture and water budgets of tropical and mid-latitude squall lines: Comparisons and sensitivity to longwave radiation. *J. Atmos. Sci.*, **50**, 673-690.
- Tao, W.-K., S. Lang, J. Simpson, C.-H. Sui and B. Ferrier and M.-D. Chou, 1996: Mechanisms of Cloud-radiation interaction in the tropics and midlatitudes. *J. Atmos. Sci.* **53**, 2624-2651.
- Tao, W.-K., J. Simpson and B. Ferrier, 1997: Cloud resolving model simulations of mesoscale convective systems, new insights and approaches to convective parameterization, Ed. D. Gregory, 77-112.
- Tao, W.-K., S. Lang, J. Simpson, W. S. Olson, D. Johnson, B. Ferrier, C. Kummerow and R. Adler, 2000a: Vertical profiles of latent heat release and their retrieval in TOGA COARE convective systems using a cloud resolving model, SSM/I and radar data, *J. Meteor. Soc. Japan*, **78**, 333-355.
- Wang, Y., W.-K. Tao, and J. Simpson, 1996: The Impact of a surface layer on a TOGA COARE cloud system development. *Mon. Wea. Rev.* **124**, 2753-2763.

- Wu, X., W. W. Grabowski and M. W. Moncrieff, 1998: Long-term behavior of cloud systems in TOGA COARE and their interactions with radiative and surface processes. Part I: Two-dimensional modeling study. *J. Atmos. Sci.*, **55**, 2693-2714.
- Xu, K.-M., and S. K. Krueger, 1991: Evaluation of cloudiness parameterizations using a cumulus ensemble model. *Mon. Wea. Rev.*, **119**, 342-367.
- Xu, K.-M., and A. Arakawa, 1992: Semiprognostic tests of the Arakawa-Schubert cumulus parameterization using simulated data. *J. Atmos. Sci.*, **49**, 2421-2436.
- Xu, K.-M., A. Arakawa, and S. Krueger, 1992: The macroscopic behavior of cumulus ensembles simulated by a cumulus ensemble model. *J. Atmos. Sci.*, **49**, 2402-2420.
- Xu, K.-M., 1994: A statistical analysis of the dependency of closure assumptions in cumulus parameterization on the horizontal resolution. *J. Atmos. Sci.*, **51**, 3674-3691.
- Xu, K.-M., 1995: Partitioning mass, heat, and moisture budgets of explicit simulated cumulus ensembles into convective and stratiform components. *J. Atmos. Sci.*, **52**, 551-573.
- Xu, K.-M., and D. A. Randall, 1996a: A semiempirical cloudiness parameterization for use in climate models. *J. Atmos. Sci.*, **53**, 3084-3102.
- Xu, K.-M., and D. A. Randall, 1996b: Explicit simulation of cumulus ensembles with the GATE Phase III data: Comparison with observations. *J. Atmos. Sci.*, **53**, 3709-3736.
- Webster, P. J., and R. Lukas, 1992: TOGA COARE: The Coupled Ocean-Atmosphere Response Experiment. *Bull. Amer. Meteor. Soc.*, **73**, 1377-1416.
- Wilhelmson, R. B., and C.-S. Chen, 1982: Numerical simulation of a cumulus ensemble in three dimensions. *J. Atmos. Sci.*, **39**, 1062-1079.
- Yanai, M., S. Esbensen, and J. Chu, 1973: Determination of average bulk properties of tropical cloud clusters from large-scale heat and moisture budgets. *J. Atmos. Sci.*, **30**, 611-627.
- Zipser, E. J., and R. H. Johnson, 1998: Systematic errors in radiosonde humidities: A global problem? Preprints, *10th Symp. on Meteorological Observations and Instrumentation*, Phoenix, AZ, Amer. Meteor. Soc., 72-73.

FIGURE CAPTIONS

- Fig. 1. Map depicting TOGA-COARE Intensive Flux Array (IFA) region.
- Fig. 2. Diagnosed IFA-mean (a) U-wind (m s^{-1}), (b) V-wind (m s^{-1}), and (c) W-velocity (cm s^{-1}).
- Fig. 3. (a) Horizontally averaged IFA diagnosed (a) apparent heating (K day^{-1}), and (b) apparent drying (g kg^{-1}) for the 19-27 December 1992 period.
- Fig. 4. Average simulated (a) Q1 (K day^{-1}), and (b) Q2 (g kg^{-1}) for experiment D.
- Fig. 5. Mean hydrometeor mixing ratios for experiment D. The fields include (a) cloud water and cloud ice combined, (b) rain water, (c) snow, and (d) graupel.
- Fig. 6. Domain-averaged snow mixing ratios for experiment D.
- Fig. 7. Mean simulated temperature deviations (K) from observations for (a) Experiment A, (b) Experiment B, (c) Experiment C, and (d) Experiment D.
- Fig. 8. Mean simulated water vapor mixing ratio deviations (g kg^{-1}) from observations for (a) Experiment A, (b) Experiment B, (c) Experiment C, and (d) Experiment D.
- Fig. 9. Root-mean-squared differences for the (a) temperature (K) and (b) water vapor mixing ratio (g kg^{-1}) for Experiment A.
- Fig. 10. Average (a) cloud fraction and (b) cloud-ice water mixing ratio (g kg^{-1}) for experiment A.

- Fig. 11. Mean (a) rain, (b) snow, and (c) graupel mixing ratios for experiment A
- Fig. 12. Average radiative heating rates (K day^{-1}) for experiment A.
- Fig. 13. Domain-averaged sensible (lower curve set) and latent heat fluxes (W m^2) for simulations in experiment A.
- Fig. 14. Mean maximum upward and downward (a) vertical velocities and (b) cloud mass fluxes for simulations in experiment A.
- Fig. 15. Domain- and time-averaged temperature deviations from IFA-diagnosed, for (a) cloudy, and (b) clear regions for experiment B.
- Fig. 16. Domain- and time-averaged water vapor deviations from IFA-diagnosed, for (a) cloudy, and (b) clear regions for experiment B.
- Fig. 17. Domain-averaged surface rainfall rates for simulations in experiment A.
- Fig. 18. X-T cross section of rainfall rates greater than 1 mm/day for simulations (a) N128, (b) C512, and (c) N1024.
- Fig. 19. Domain-averaged contour plots of $Q1$ (K day^{-1}) and $Q2$ (K day^{-1}) for (a) simulated, and (b) TOGA-COARE IFA diagnosed regions.
- Fig. 20. Mean (a) major, and (b) minor components of the $Q1$ (K day^{-1}) budget for case C512.
- Fig. 21. Mean components of the $Q2$ (g kg^{-1}) budget for case C512.

- Fig. 22. Domain-averaged (a) $Q1$ ($K \text{ day}^{-1}$) and (b) $Q2$ ($K \text{ day}^{-1}$) budgets in convective and stratiform regions for case C512.
- Fig. 23. Domain-averaged (a) graupel and cloud water mixing ratios ($g \text{ kg}^{-1}$) in convective regions, and (b) snow and rain mixing ratios ($g \text{ kg}^{-1}$) in stratiform regions for case C512.
- Fig. 24. (a) Domain-averaged, and (b) mean profiles of the total, convective, and stratiform mass fluxes ($kg \text{ m}^{-2} \text{ s}^{-1}$) for case C512.
- Fig. 25. Cross-sectional hydrometeor mixing ratio field contours ($g \text{ kg}^{-1}$) for case C512 at 143 hours. The contour intervals are 0.01, 0.1, 0.2, 0.5, 1.0, 2.0, 5.0, and 10.0 $g \text{ kg}^{-1}$.
- Fig. 26. Observed and domain-averaged simulated total, convective, and stratiform surface rainfall rates ($mm \text{ day}^{-1}$) for case C512.
- Fig. 27. X-T cross sections of rainfall rates greater than 1 mm/day for (a) convective, and (b) stratiform regions for case C512.
- Fig. 28. Domain-averaged plots of observed (thick solid lines) and simulated (thin solid lines) latent (upper curves) and sensible (lower curves) heat flux (left scale; $W \text{ m}^{-2}$), and mean wind speed (dashed line), and wind speed standard deviation (dotted line) at the surface (right scale; $m \text{ s}^{-1}$) for the control case C512.

TABLES

- Table 1. Key developments in the Cloud-Ensemble Model (CEM) approach over the past two decades.
- Table 2. Experiments conducted in this study. Note that C512 is common to all four experiments.
- Table 3. Total mean rainfall amounts for all experiments.
- Table 4. Mean sensible heat flux (W m^{-2}) for the simulations in experiment A.
- Table 5. Individual terms of the column temperature budget (K) for simulations in experiment A. The letters in the heading correspond to the corresponding components in the temperature equation shown above.
- Table 6. Individual terms of the column moisture budget (mm) for simulations in experiment A. The letters in the heading correspond to the corresponding components in the moisture equation shown above.
- Table 7. Domain-mean total, convective, and stratiform surface rainfall (mm) and convective/stratiform percentage for case C512.

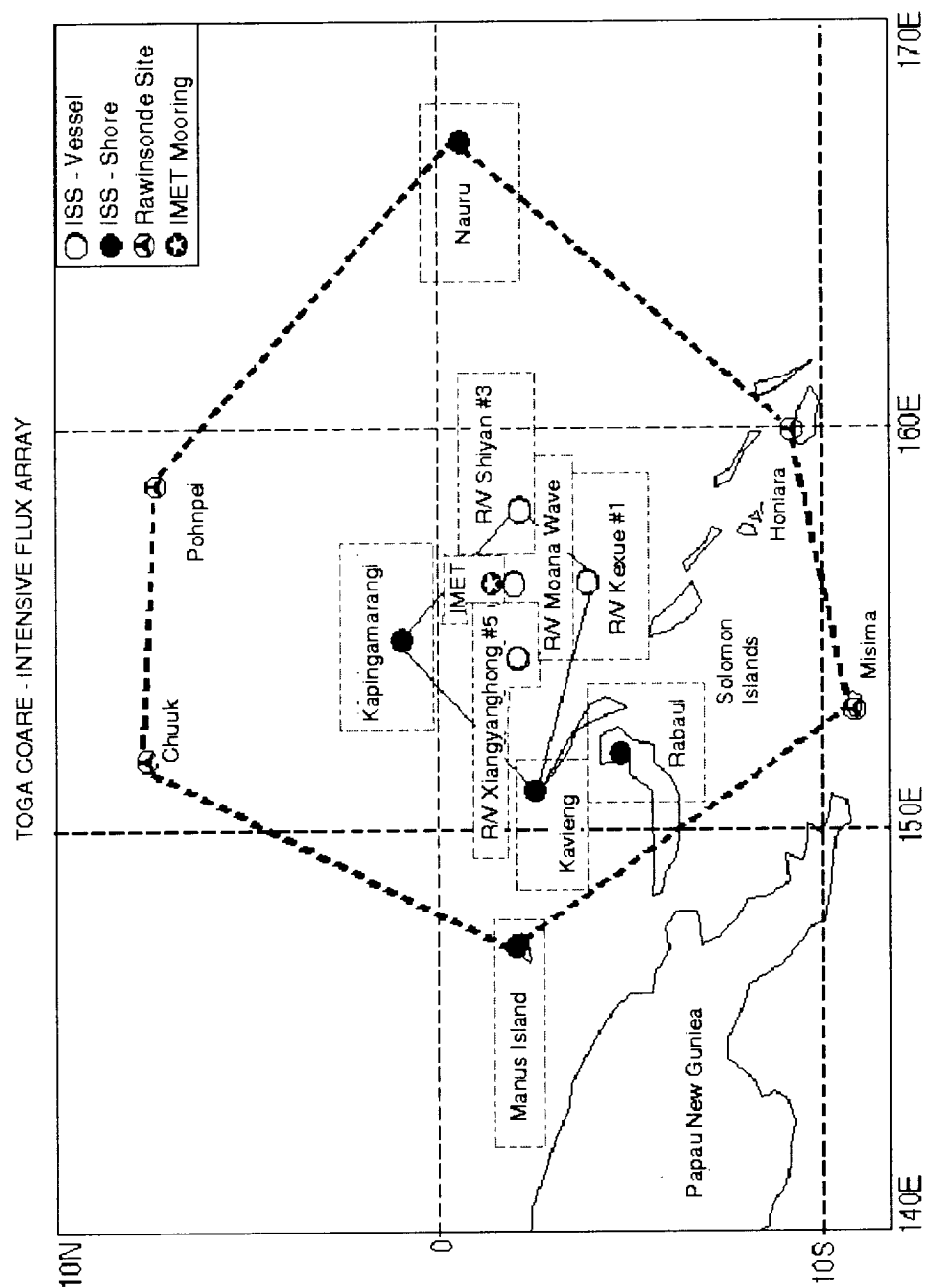


Fig. 1. Map depicting TOGA-COARE Intensive Flux Array (IFA) region.

	Model	Microphysics	Turbulence	Domain	Integration
Soong & Ogura (1980)	2-D	Water	TKE	64 km	24 h
Soong & Tao (1980)	2-D	Water	TKE	64 km	24 h
Soong & Tao (1984)	2-D	Water	TKE	128 km	6 h
Ogura & Jiang (1985)	2-D	Water	TKE	128 km	16 h
Tao & Soong (1986)	3-D	Water	TKE	32 x 32 km ²	6 h
Lipps & Helmer (1986)	2-D 3-D	Water	K-theory	32-64 km 24 x 16 km ²	4 h
Tao, Simpson & Soong (1987)	2-D 3-D	Water	TKE	128 km 32 x 32 km ²	6 h 6 h
Nikajima & Matsuno (1988)	2-D	Water	K-theory	512 km	50 h
Dudhia & Moncrieff (1987)	3-D	Water	Prescribed fluxes	25 x 50 km ²	3 h
Krueger (1988)	2-D	Water	3rd Moment	30 km	2 h
Tao & Simpson (1989a, b)	2-D 3-D	Water & Ice	TKE	512 km 96 x 96 km ²	12 h 4 h
Gregory & Miller (1989)	2-D	Water	Prescribed fluxes	256 km	9 h
Xu & Krueger (1991)	2-D	Water & Ice	3rd moment	512 km	120 h
McCumber, Tao, Simpson, Penc & Soong (1992)	2-D 3-D	Water Water & Ice	TKE	512 km 64 x 32 km ²	12 h 3 h
Xu, Arakawa & Krueger (1992), Xu and Arakawa (1992), Xu (1994)	2-D	Water & Ice	3rd moment	512 km	120 h
Held, Hemler & Ramaswamy (1993)	2-D	Water & Ice	K-theory	640 km	1000 h
Sui, Lau, Tao, Simpson & Chou (1994)	2-D	Water & Ice	TKE	768 km	1248 h
Grabowski, Wu & Moncrieff (1996,1999) & Grabowski, Wu Moncrieff & Hall (1998)	2-D 3-D	Water & Ice	K-theory	900 km 400 x 400 km ²	7 days
Xu (1995), Xu and Randall (1996a,b)	2-D	Water & Ice	3rd Moment	512 km	18 days
Donner, Seman & Hemler (1999)	3-D	Water & Ice	K-theory	220 x 200 km ²	73 h
Xu, Grabowski & Moncrieff (1998)	2-D	Water & Ice	K-theory	900 km	39 days
Li, Sui, Lau & Chou (1999)	2-D	Water & Ice	TKE	768 km	7 days
Su, Chen & Bretherton (1999)	3-D	Water & Ice	Blackadar-Type	210 x 210 km ²	7 days
Johnson, Tao, Simpson & Sui (2000)	2-D	Water & Ice	TKE	1024 km	7 days

Table 1. Key developments in the Cloud-Ensemble Model (CEM) approach over the past two decades.

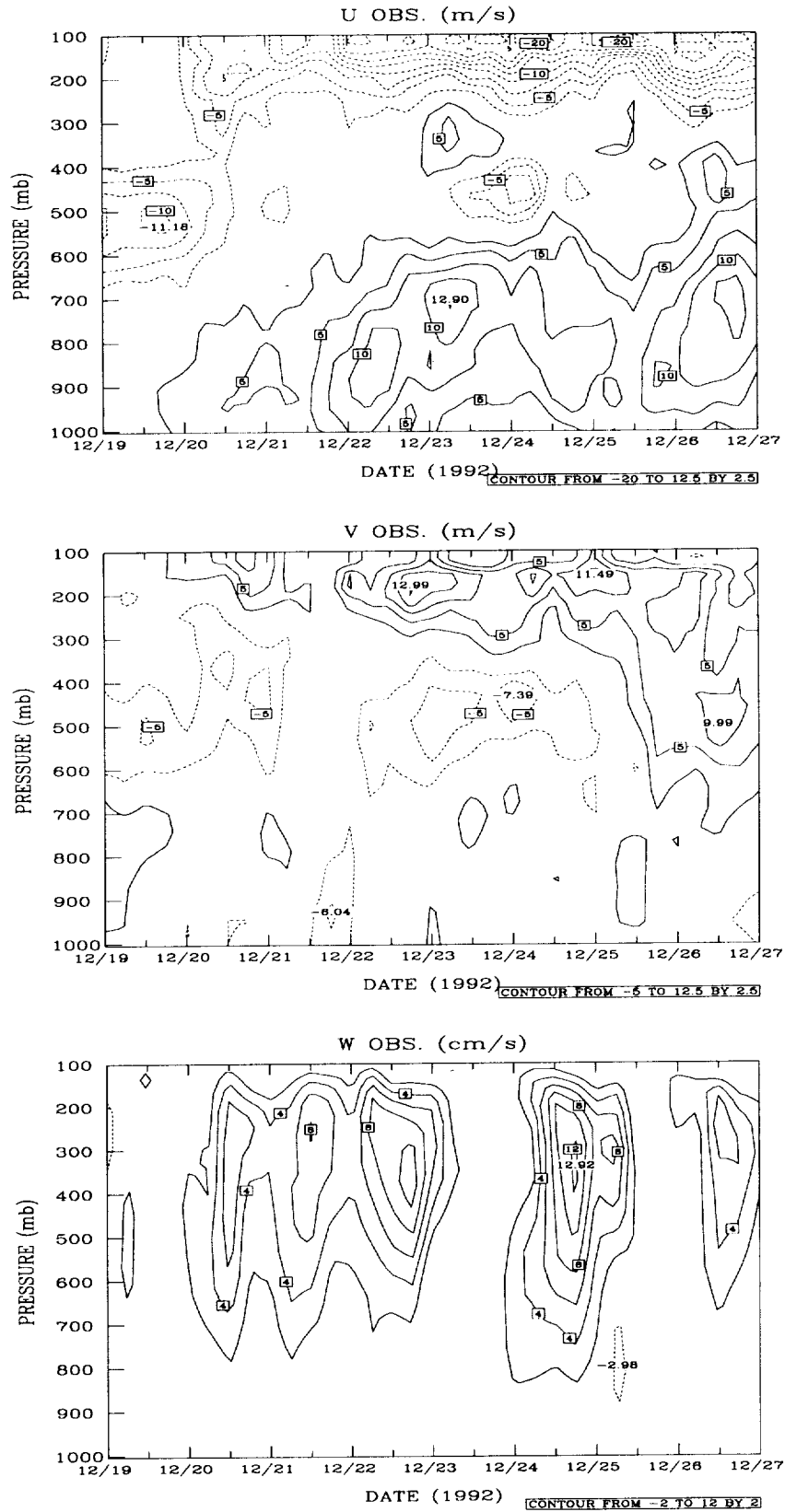


Fig. 2. Diagnosed IFA-mean (a) U-wind (m s^{-1}), (b) V-wind (m s^{-1}), and (c) W-velocity (cm s^{-1}).

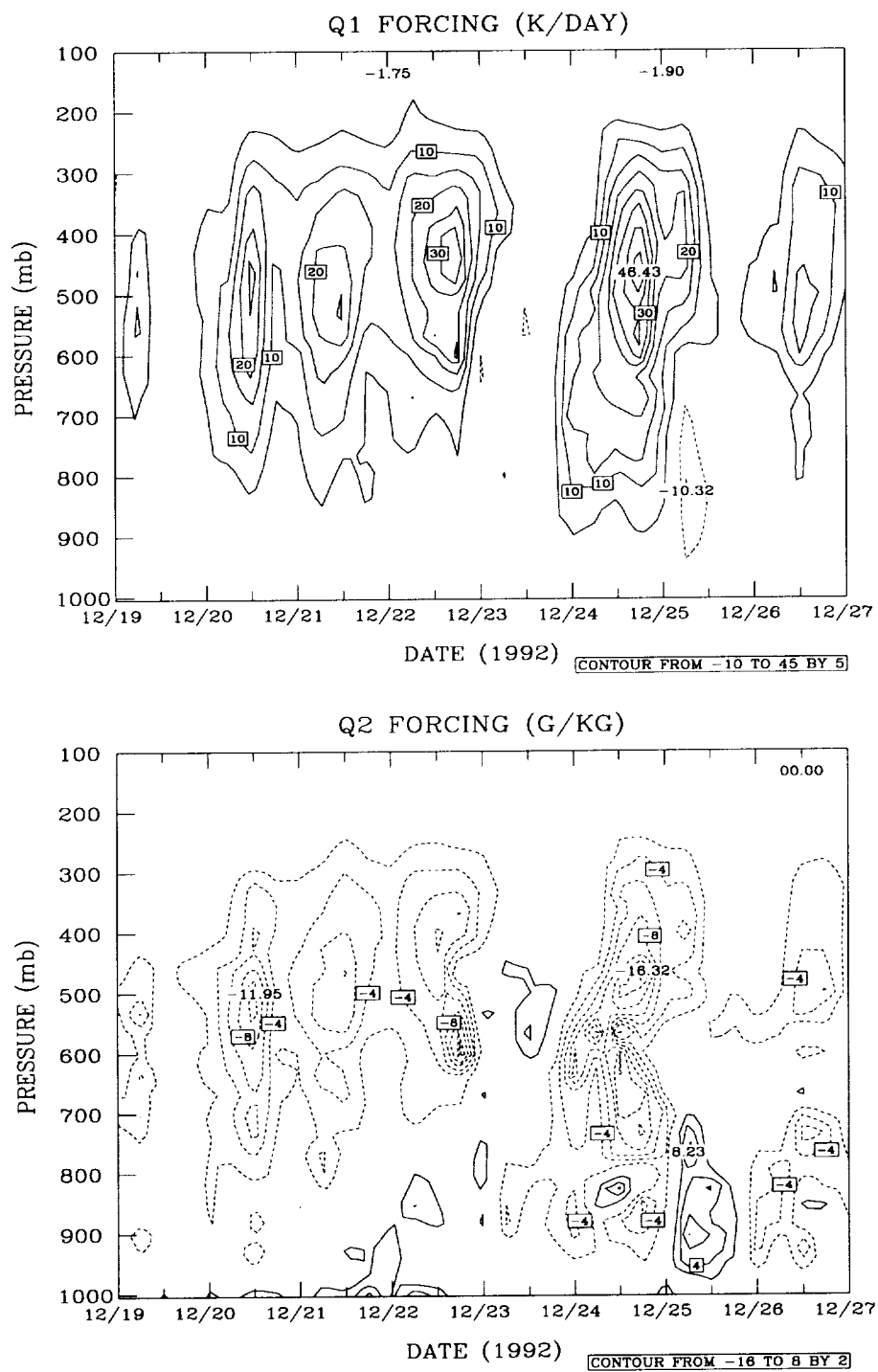


Fig. 3. (a) Horizontally averaged IFA diagnosed (a) apparent heating (K day^{-1}), and (b) apparent drying (g kg^{-1}) for the 19-27 December 1992 period.

	Simulation	Number Horizontal Points	Horizontal Spacing (m)	Number Vertical Points	Vertical Spacing (m)	Positive Definite (ON/OFF)
A	N128	128	1000	41	80-1000	ON
	C512	512	1000	41	80-1000	ON
	N1024	1024	1000	41	80-1000	ON
B	DX500	1024	500	41	80-1000	ON
	C512	512	1000	41	80-1000	ON
	DX2000	256	2000	41	80-1000	ON
C	Z32	512	1000	32	126-1200	ON
	C512	512	1000	41	80-1000	ON
	Z53	512	1000	50	50-750	ON
D	PDOFF	512	1000	41	80-1000	OFF
	C512	512	1000	41	80-1000	ON
	VFILT4	512	1000	41	80-1000	OFF*

Table2. Experiments conducted in this study. Note that C512 is common to all four experiments.

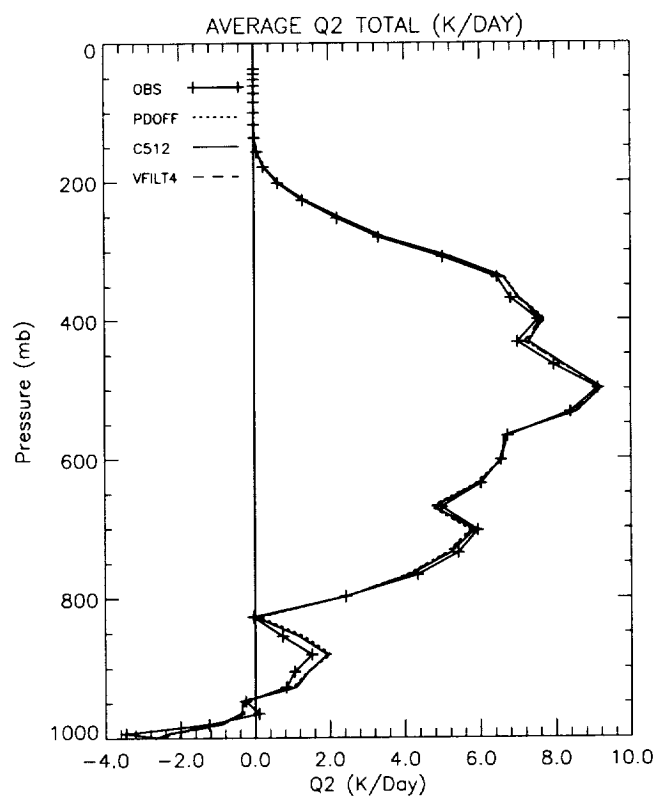
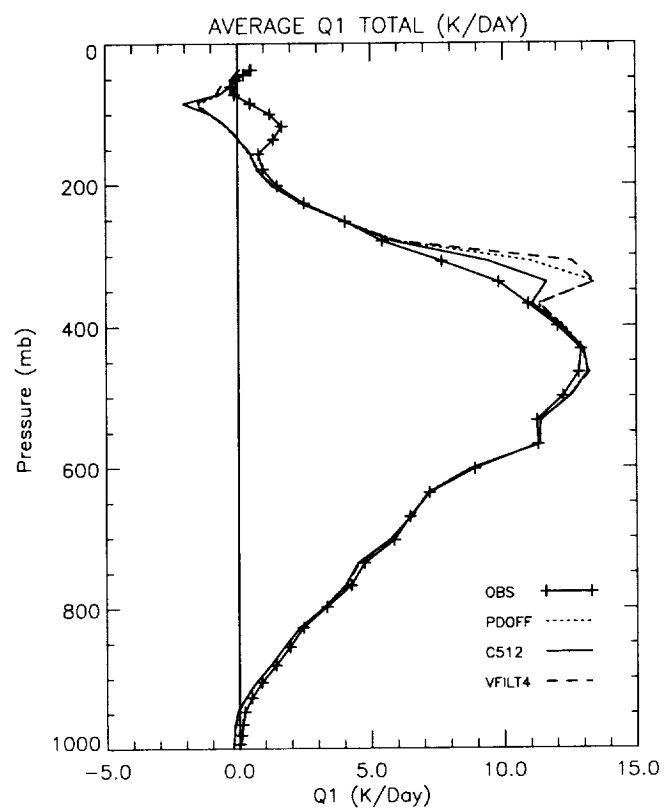


Fig. 4. Average simulated (a) Q1 (K day^{-1}), and (b) Q2 (g kg^{-1}) for experiment D.

Simulation	Total Rainfall (mm)
OBS	160.8
N128	157.8
C512	161.6
N1024	165.1
DX500	161.0
C512	161.6
DX2000	163.5
Z32	163.1
C512	161.6
Z53	162.4
PDOFF	163.7
C512	161.6
VFILT4	163.1

Table 3. Total mean rainfall amounts for all experiments.

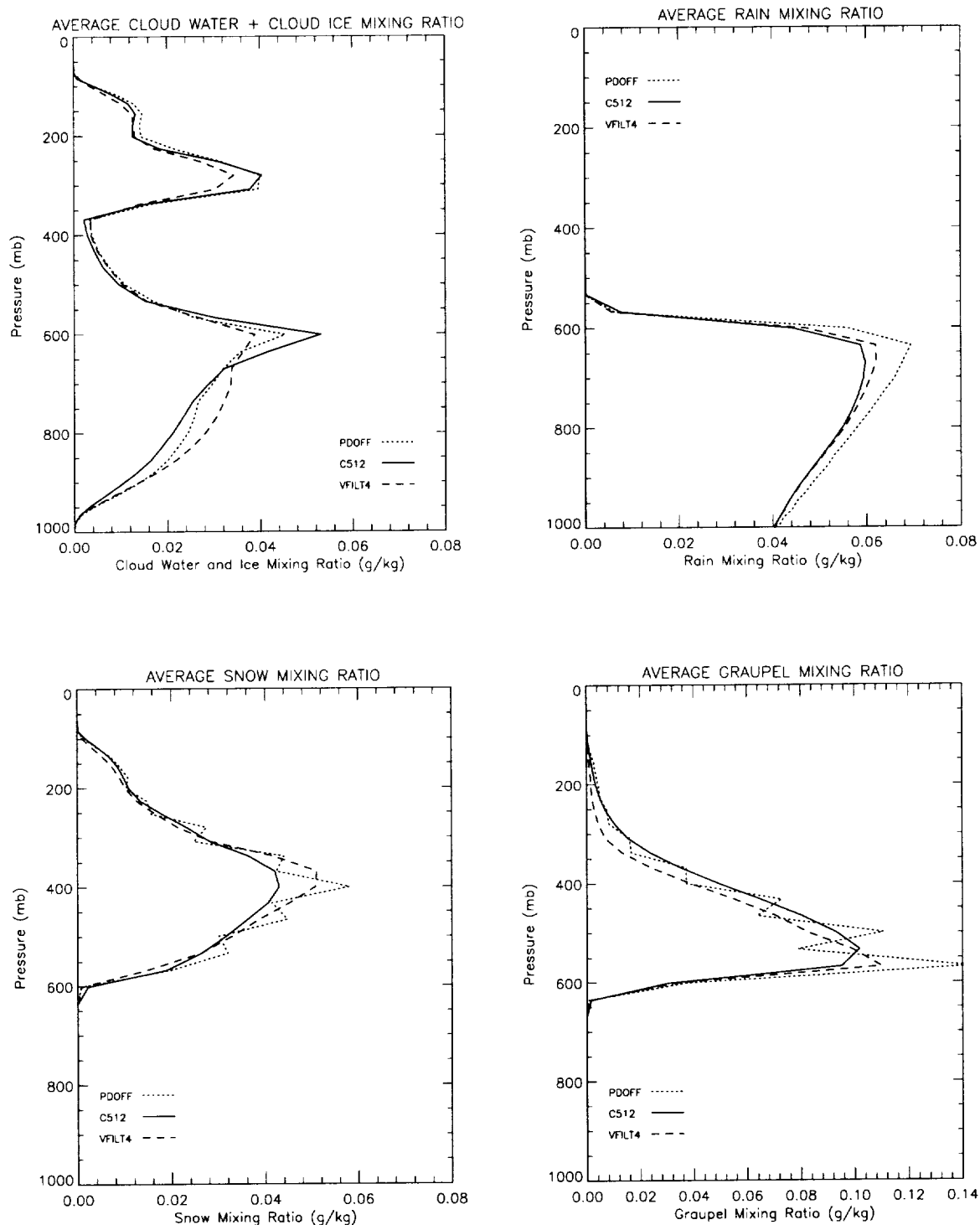


Fig. 5. Mean hydrometeor mixing ratios for experiment D. The fields include (a) cloud water and cloud ice combined, (b) rain water, (c) snow, and (d) graupel.

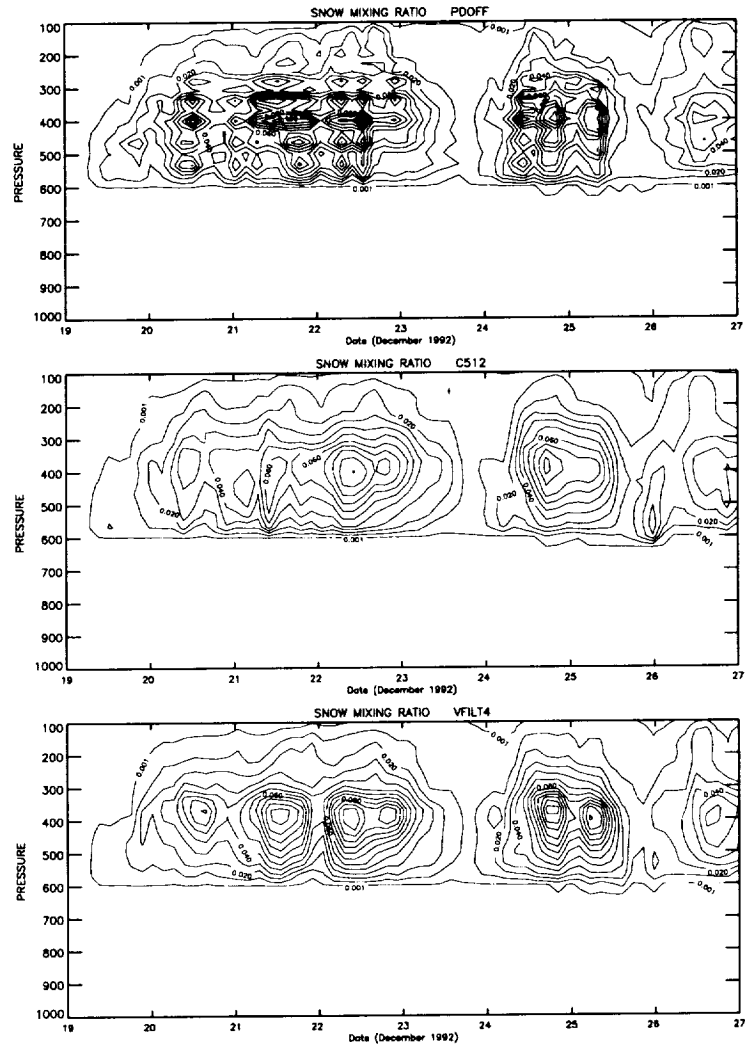


Fig. 6. Domain-averaged snow mixing ratios for experiment D.

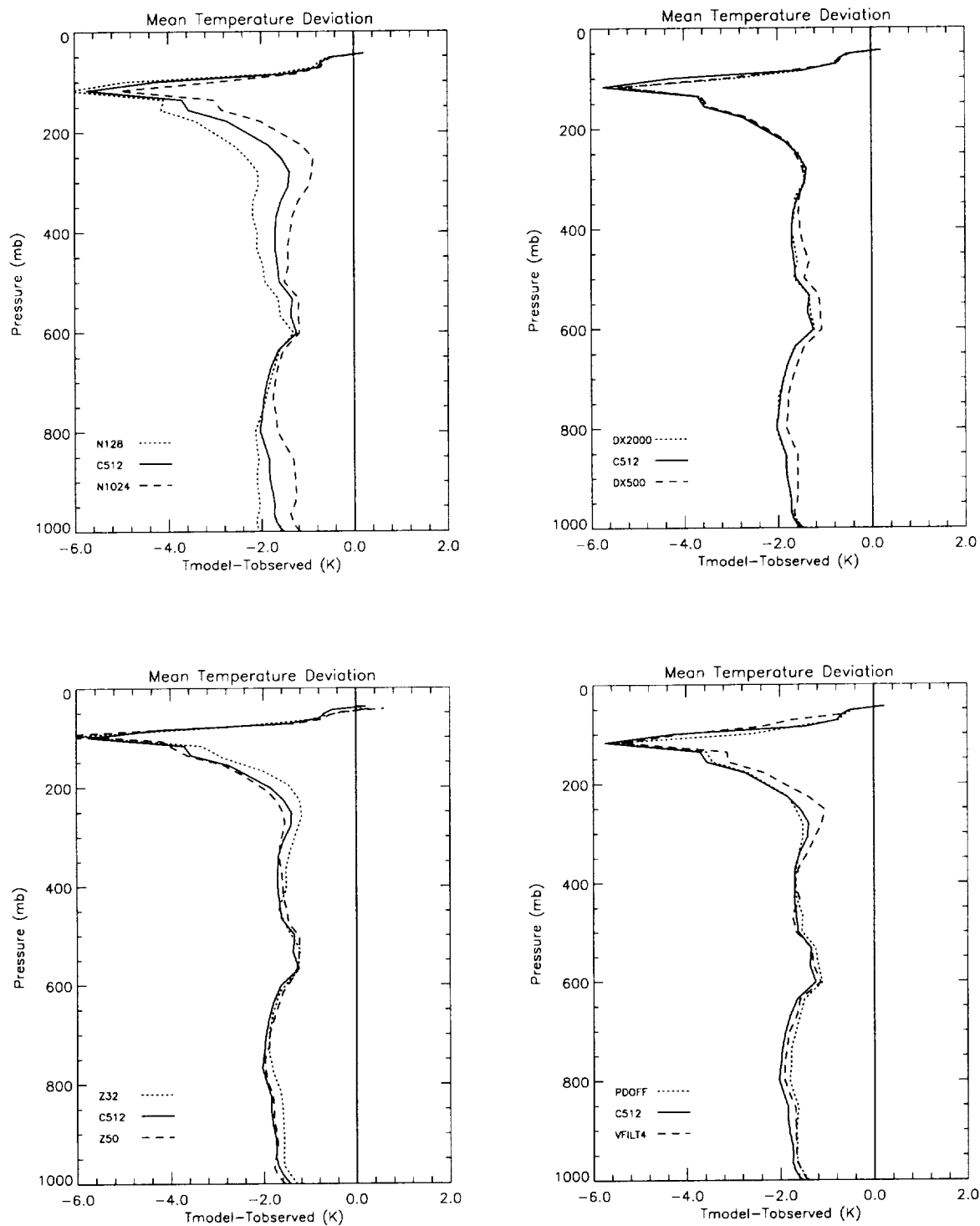


Fig. 7. Mean simulated temperature deviations (K) from observations for (a) Experiment A, (b) Experiment B, (c) Experiment C, and (d) Experiment D.

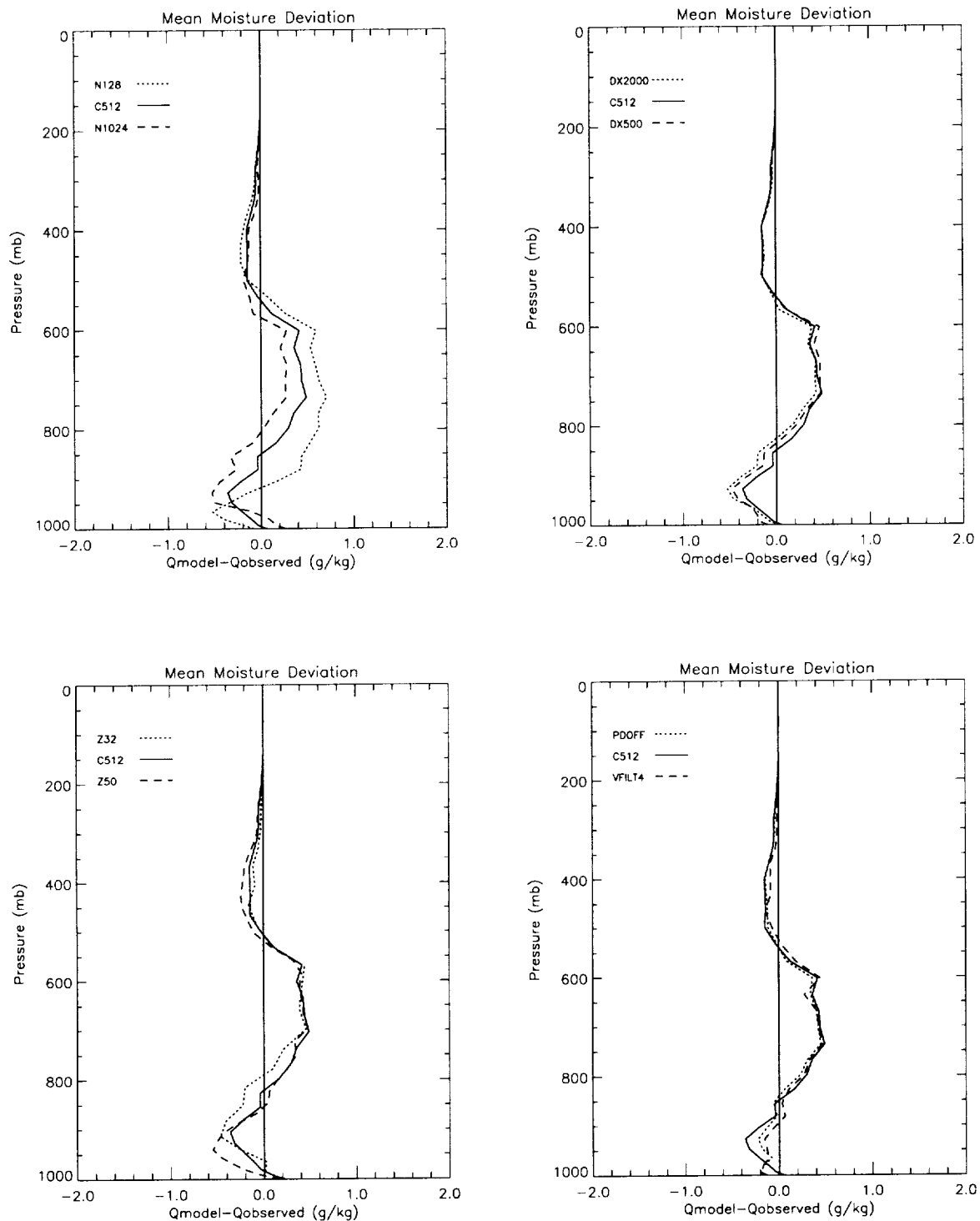


Fig. 8. Mean simulated water vapor mixing ratio deviations (g kg^{-1}) from observations for (a) Experiment A, (b) Experiment B, (c) Experiment C, and (d) Experiment D.

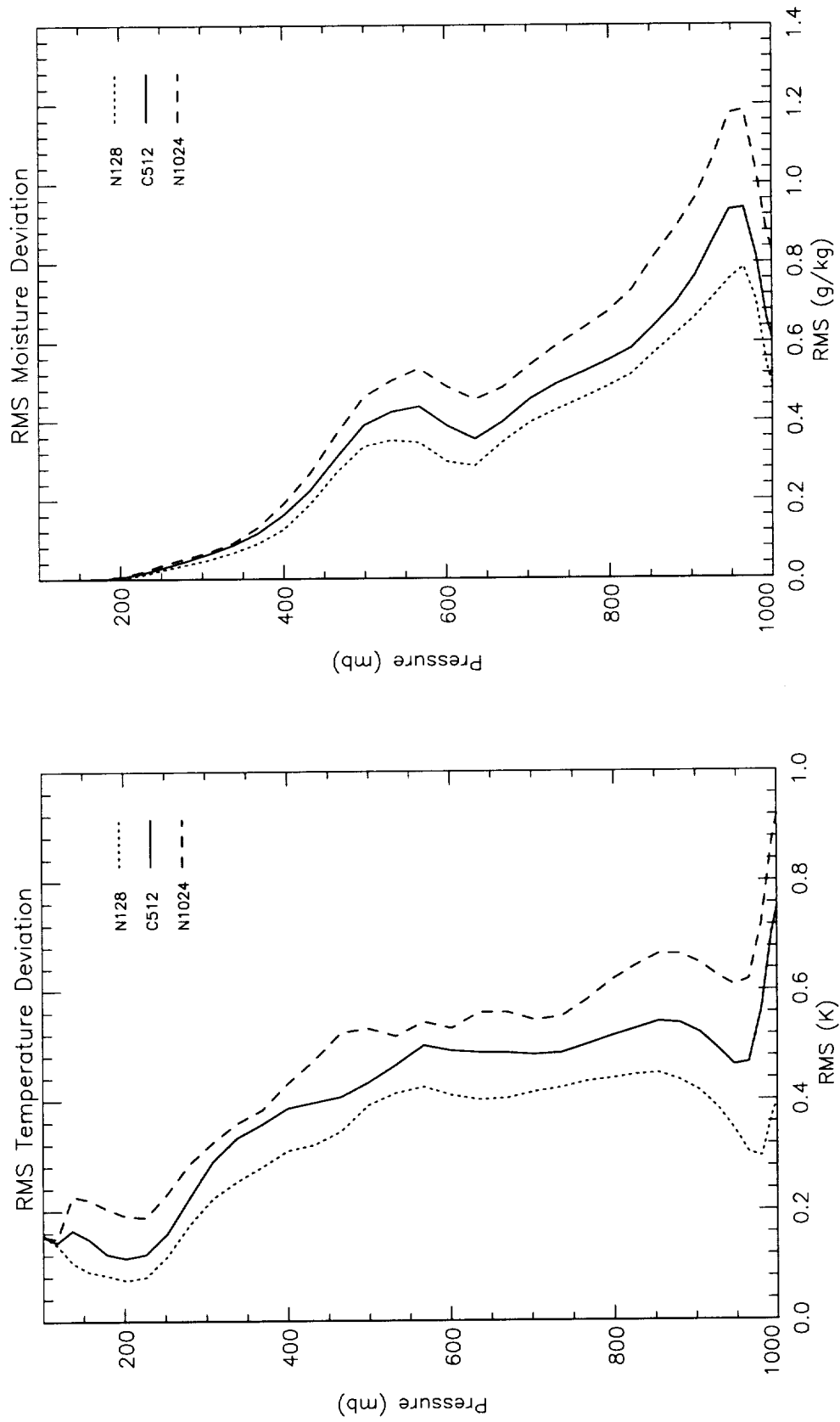


Fig. 9. Root-mean-squared differences for the (a) temperature (K) and (b) water vapor mixing ratio (g kg^{-1}) for Experiment A.

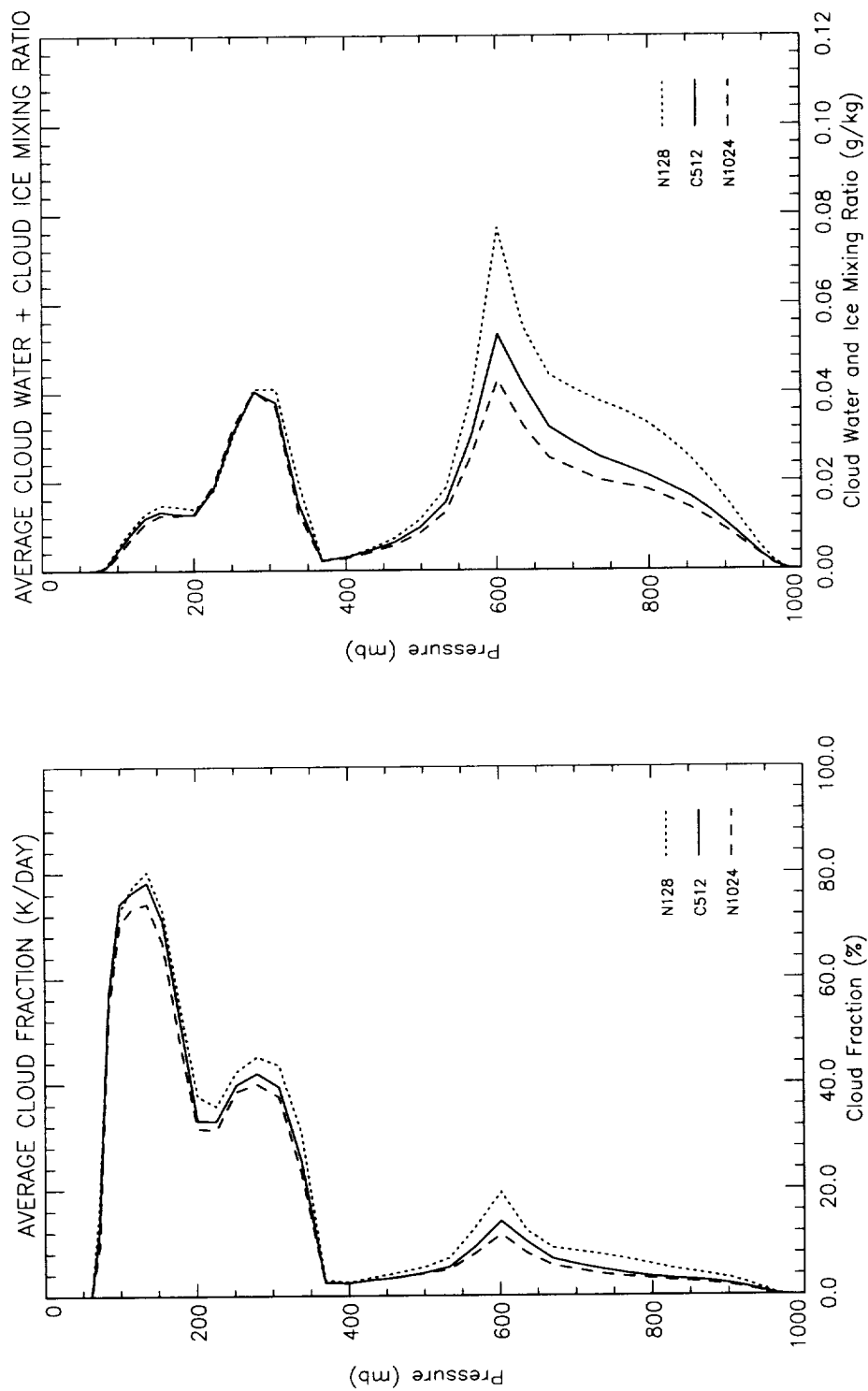
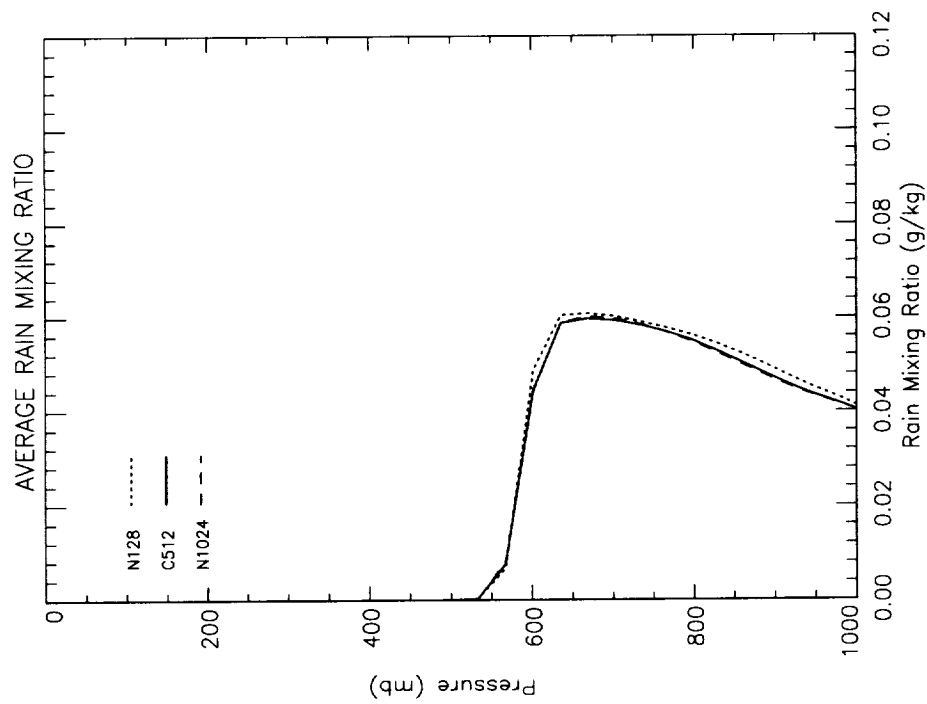
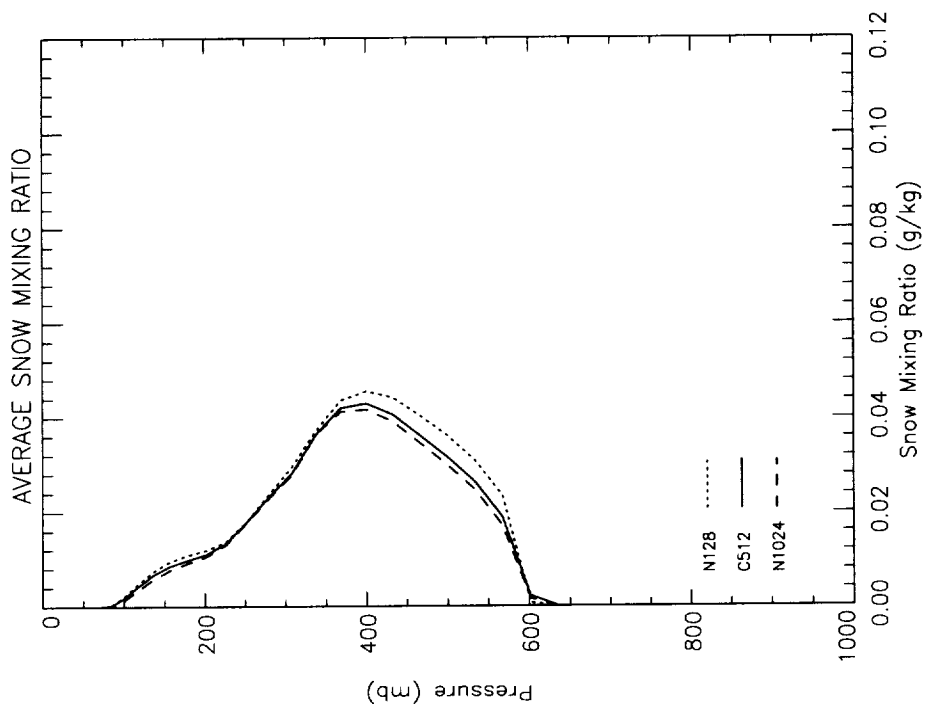


Fig. 10. Average (a) cloud fraction and (b) cloud-ice water mixing ratio (g kg^{-1}) for experiment A.



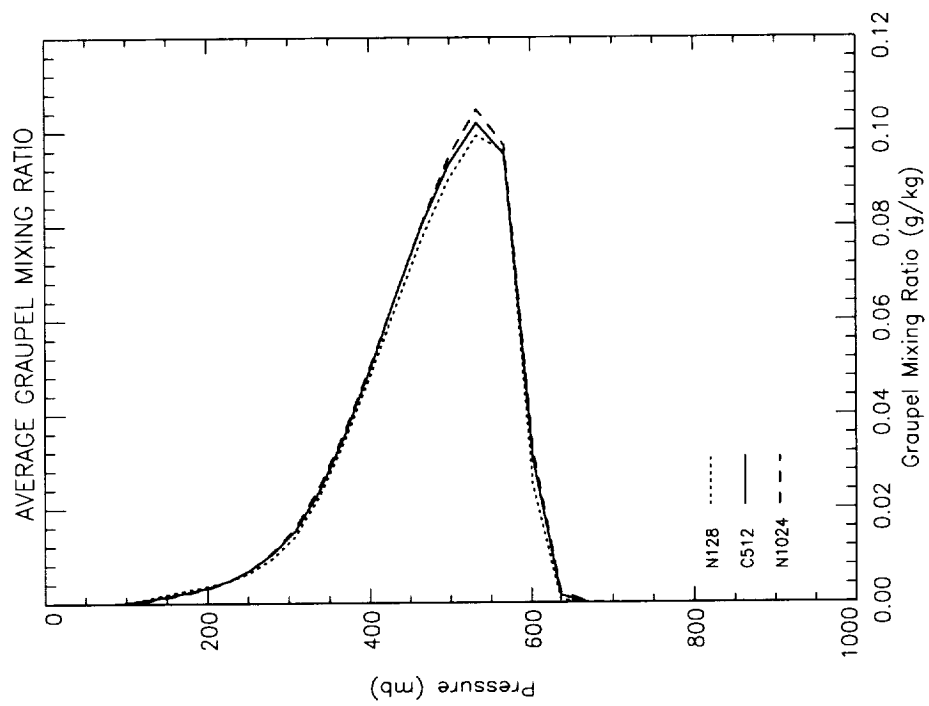


Fig. 11. Mean (a) rain, (b) snow, and (c) graupel mixing ratios for experiment A

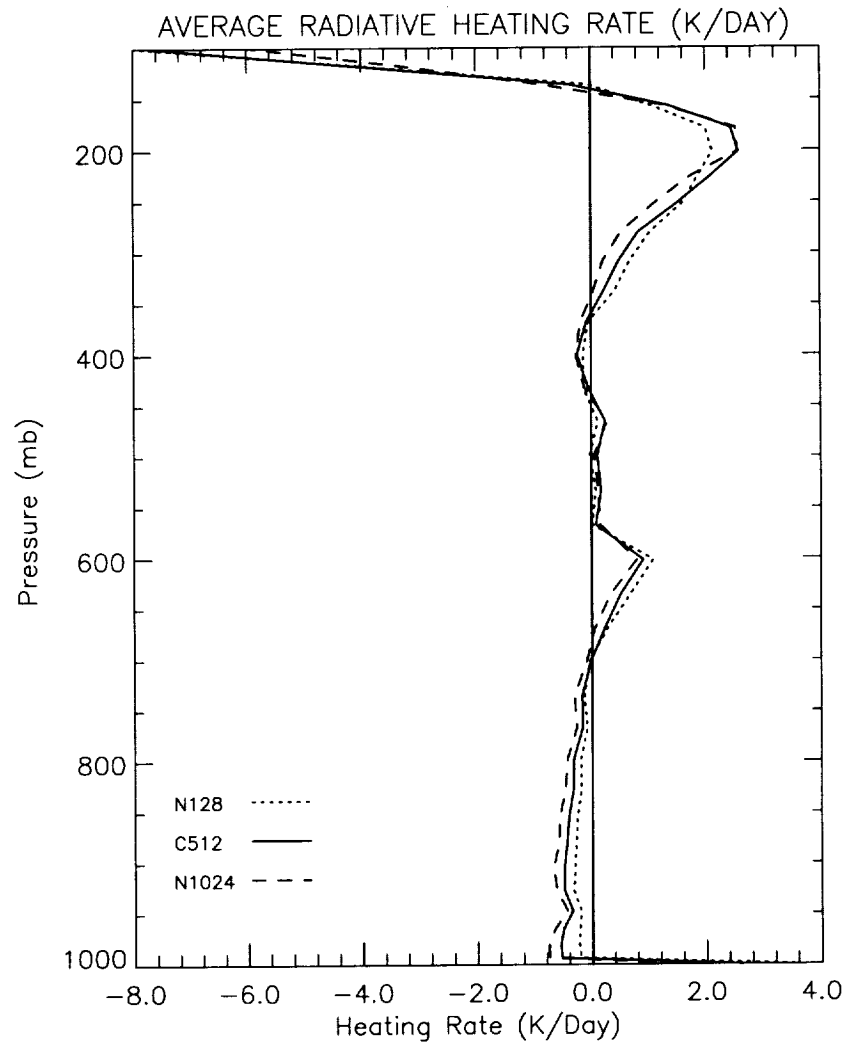


Fig. 12. Average radiative heating rates (K day^{-1}) for experiment A.

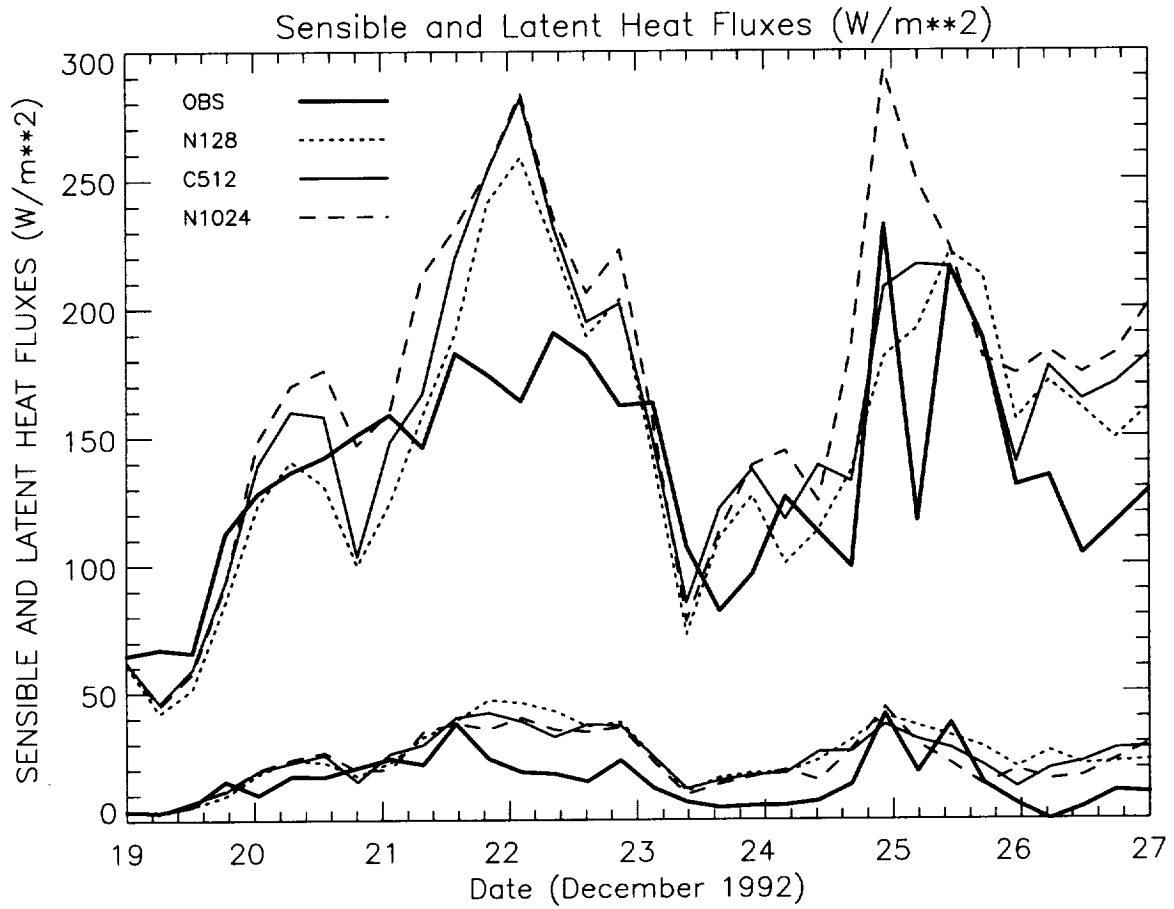


Fig. 13. Domain-averaged sensible (lower curve set) and latent heat fluxes (W m^{-2}) for simulations in experiment A.

Simulation	Mean Sensible Heat Flux (W m^{-2})	Mean Latent Heat Flux (W m^{-2})
OBS	14.88	136.91
N128	25.11	147.95
C512	23.76	158.24
N1024	22.75	172.09

Table 4. Mean sensible heat flux (W m^{-2}) for the simulations in experiment A.

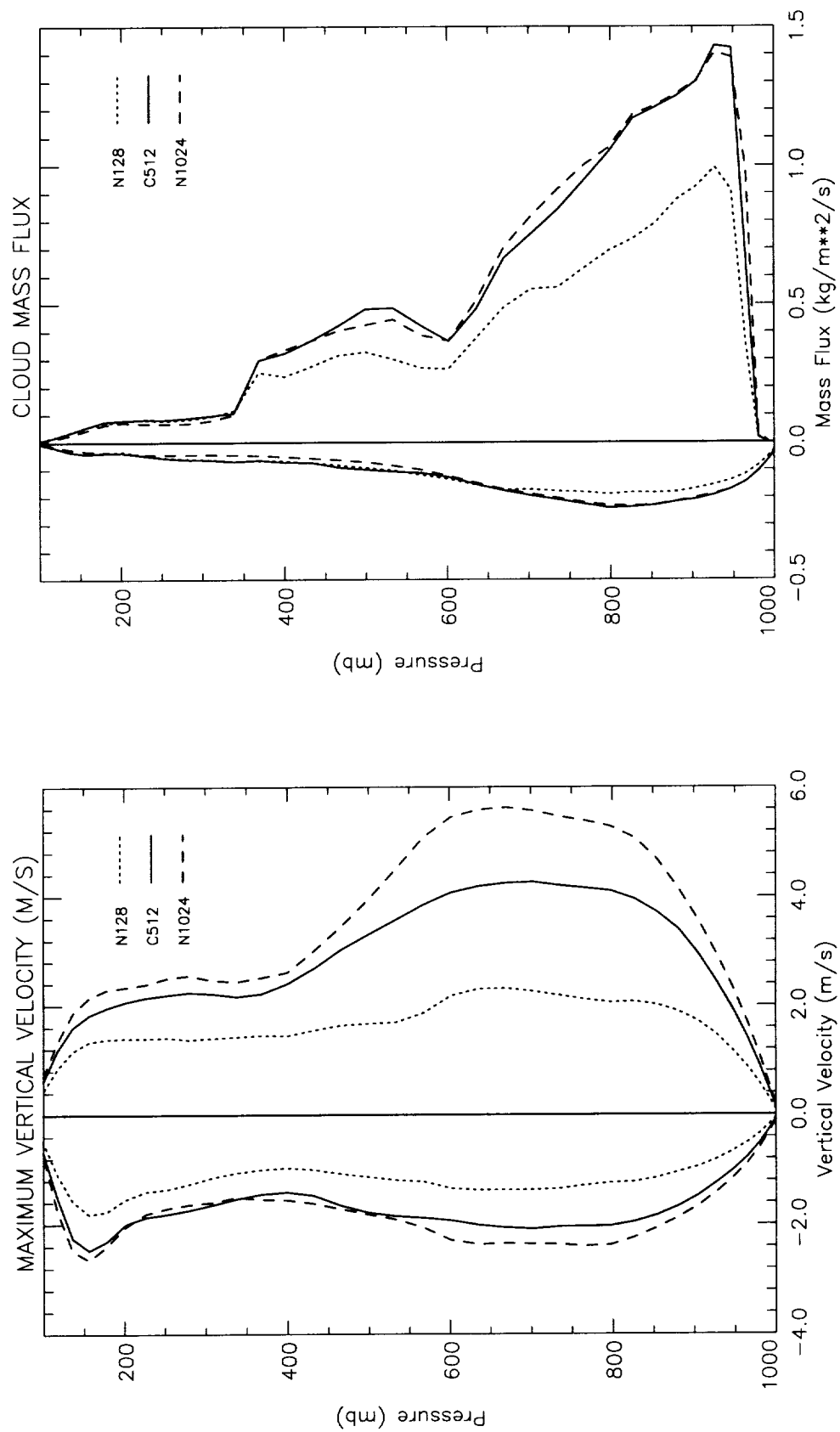


Fig. 14. Mean maximum upward and downward (a) vertical velocities and (b) cloud mass fluxes for simulations in experiment A.

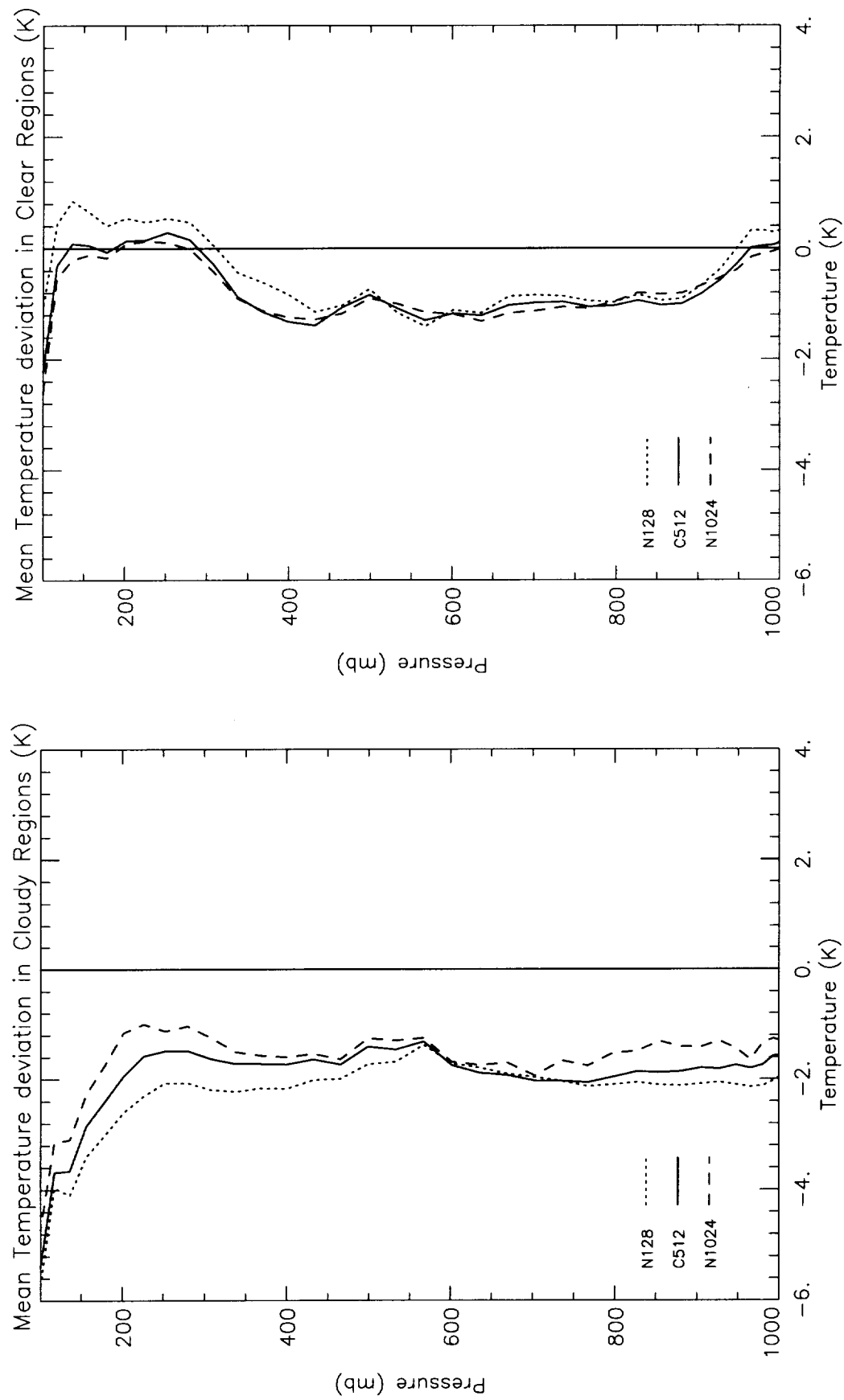


Fig. 15. Domain- and time-averaged temperature deviations from IFA-diagnosed, for (a) cloudy, and (b) clear regions for experiment B.

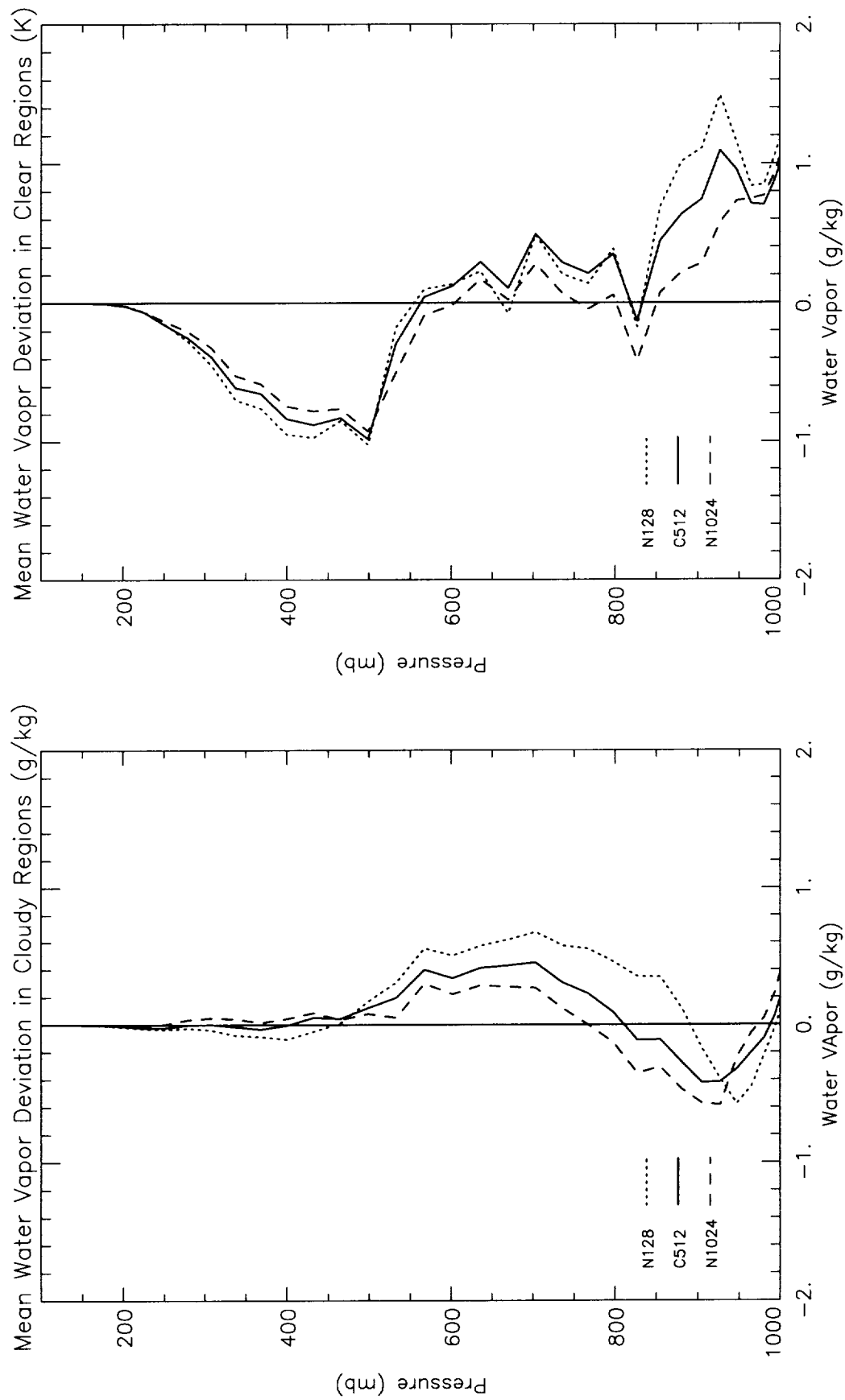


Fig. 16. Domain- and time-averaged water vapor deviations from IFA-diagnosed, for (a) cloudy, and (b) clear regions for experiment B.

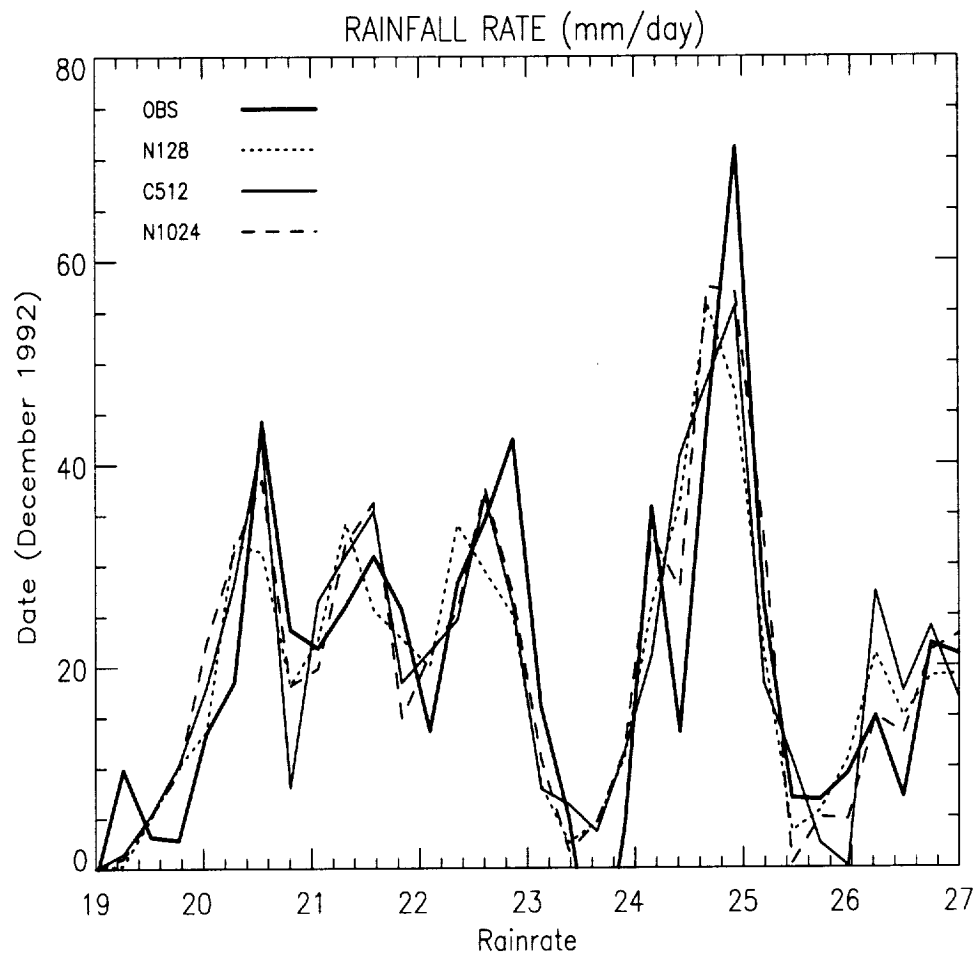


Fig. 17. Domain-averaged surface rainfall rates for simulations in experiment A.

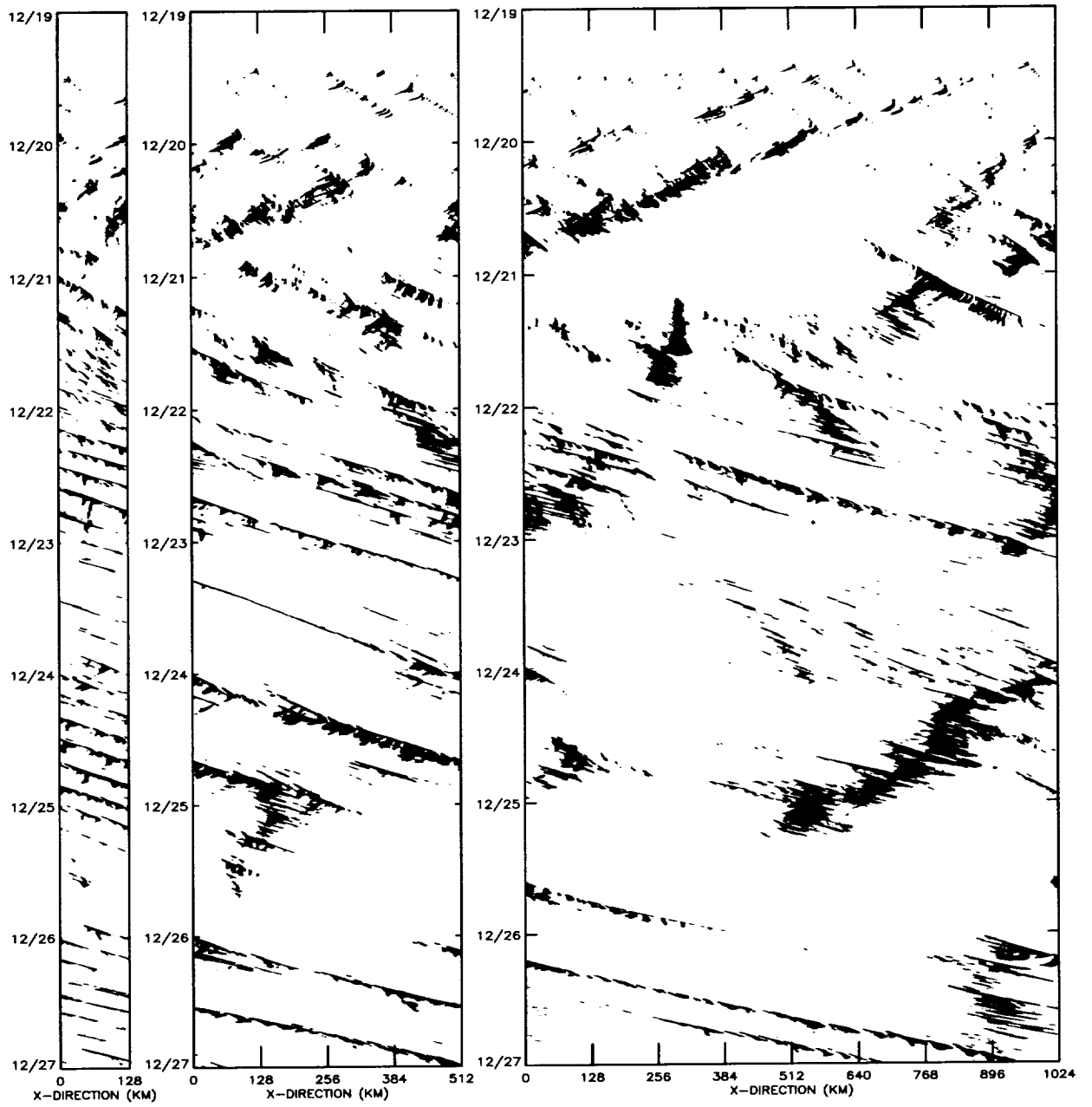


Fig. 18. X-T cross section of rainfall rates greater than 1 mm/day for simulations (a) N128, (b) C512, and (c) N1024.

$$\langle \frac{\partial \bar{\rho} \bar{T}}{\partial t} \rangle = \underbrace{\langle \frac{L_v}{C_p} \bar{\rho} (\bar{c} - \bar{e}) \rangle}_A + \underbrace{\langle \frac{L_s}{C_p} \bar{\rho} (\bar{d} - \bar{s}) \rangle}_B + \underbrace{\langle \bar{\rho} \frac{L_f}{C_p} (\bar{f} - \bar{m}) \rangle}_C - \underbrace{\langle \bar{w} \frac{\partial \bar{\rho} \bar{T}}{\partial z} \rangle}_D + \underbrace{\frac{1}{C_p} \langle Q_R \rangle + \bar{H}_s}_E$$

Simulation	A	B	C	D	E
N128	-2.84	48.96	-55.17	0.28	1.76
C512	-2.24	49.97	-55.17	0.00	1.65
N1024	-1.73	51.07	-55.17	-0.44	1.57
N1024-N128	1.11	2.11	0	-0.72	-0.19

Table 5. Individual terms of the column temperature budget (K) for simulations in experiment A. The letters in the heading correspond to the corresponding components in the temperature equation shown above.

$$L_v \langle \frac{\partial \bar{\rho} \bar{q}_v}{\partial t} \rangle = - \underbrace{\langle L_v \bar{\rho} (\bar{c} - \bar{e}) \rangle}_A + \underbrace{\langle L_s \bar{\rho} (\bar{d} - \bar{s}) \rangle}_B - \underbrace{\langle L_v \bar{w} \frac{\partial \bar{\rho} \bar{q}_v}{\partial z} \rangle}_C + \underbrace{L_v \bar{E}_o}_D$$

Simulation	A	B	C	D
N128	4.68	-156.91	120.22	41.38
C512	2.95	-161.07	120.22	43.80
N1024	3.05	-164.69	120.22	47.52
N1024-N128	-1.63	-7.78	0	6.14

Table 6. Individual terms of the column moisture budget (mm) for simulations in experiment A. The letters in the heading correspond to the corresponding components in the moisture equation shown above.

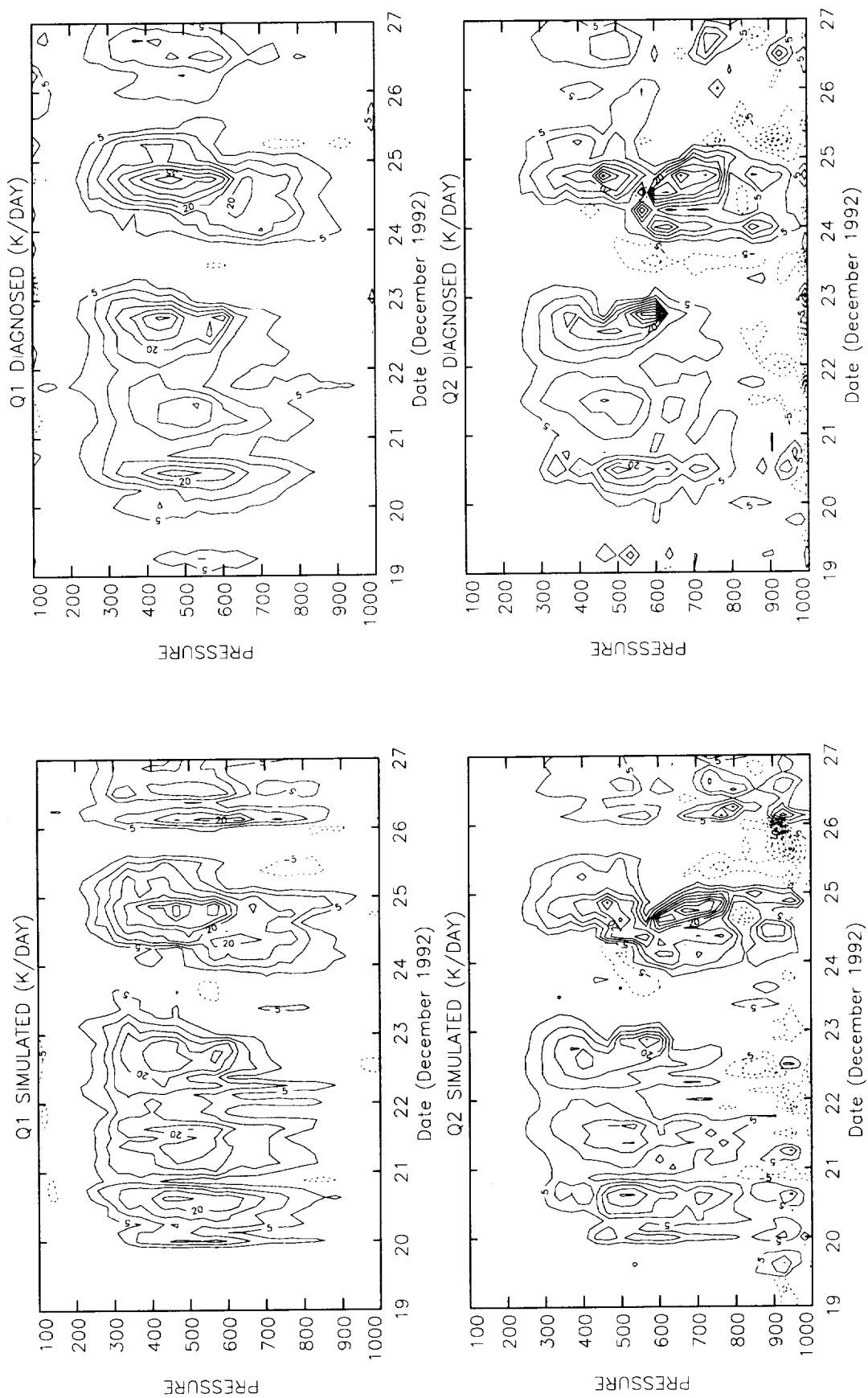


Fig. 19. Domain-averaged contour plots of Q1 (K day^{-1}) and Q2 (K day^{-1}) for (a) simulated, and (b) TOGA-COARE IFA diagnosed regions.

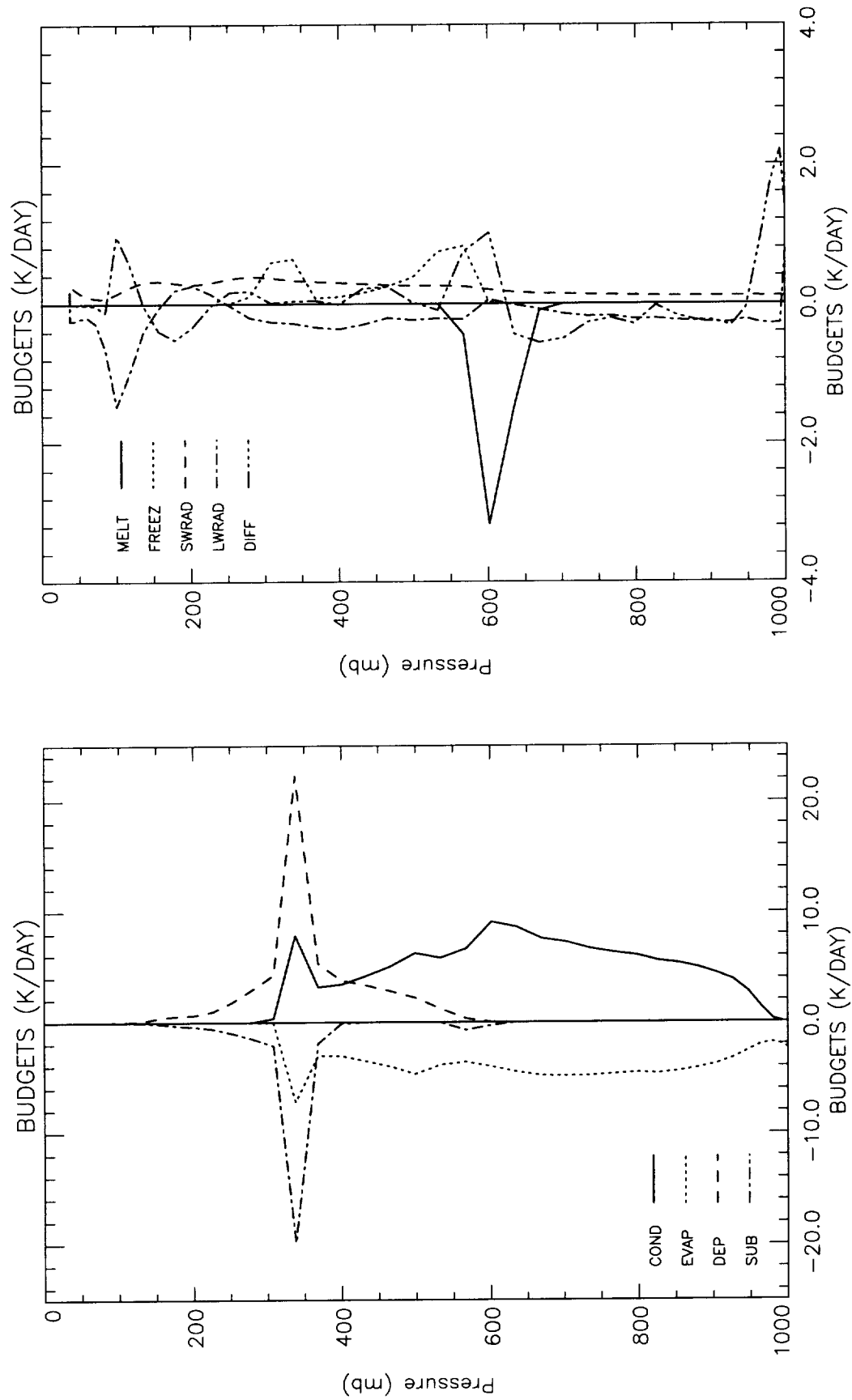


Fig. 20. Mean (a) major, and (b) minor components of the Q1 (K day^{-1}) budget for case C512.

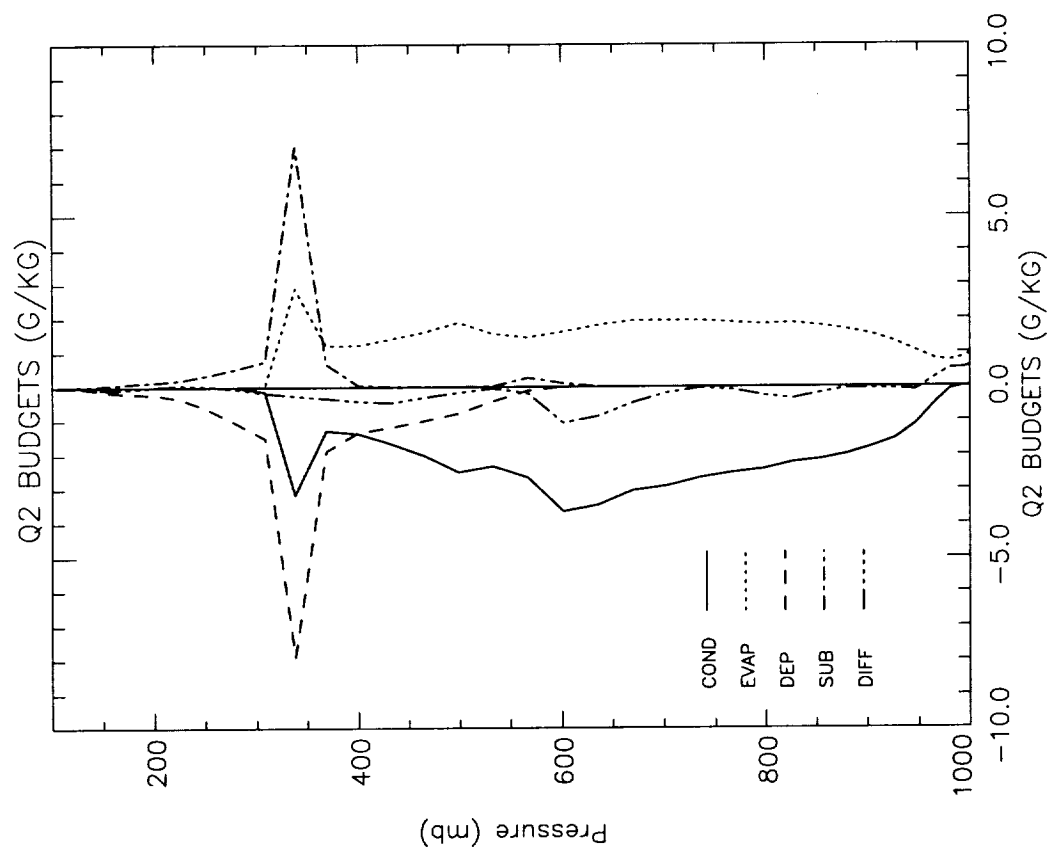


Fig. 21. Mean components of the Q2 (g kg^{-1}) budget for case C512.

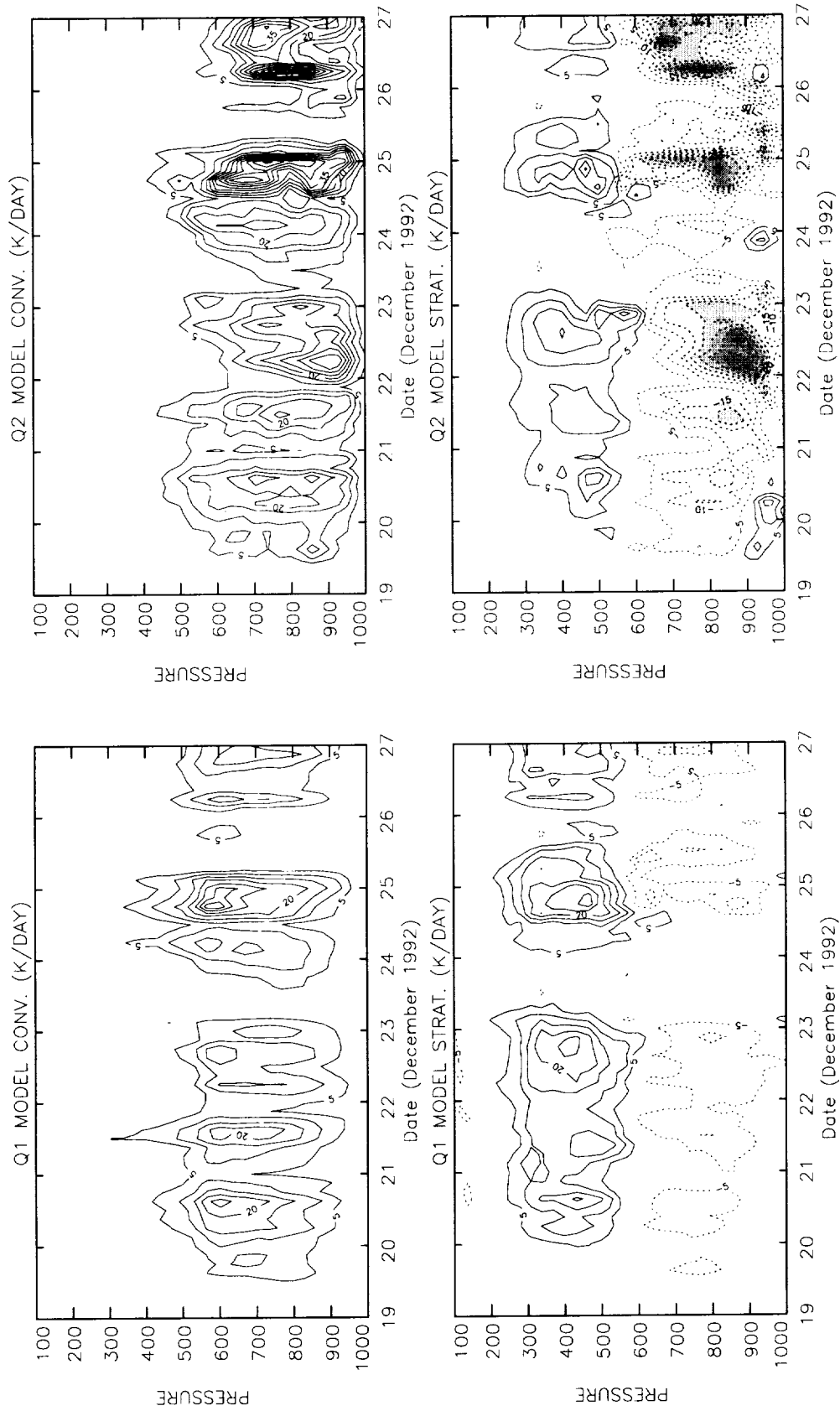


Fig. 22. Domain-averaged (a) Q1 (K day⁻¹) and (b) Q2 (K day⁻¹) budgets in convective and stratiform regions for case C512.

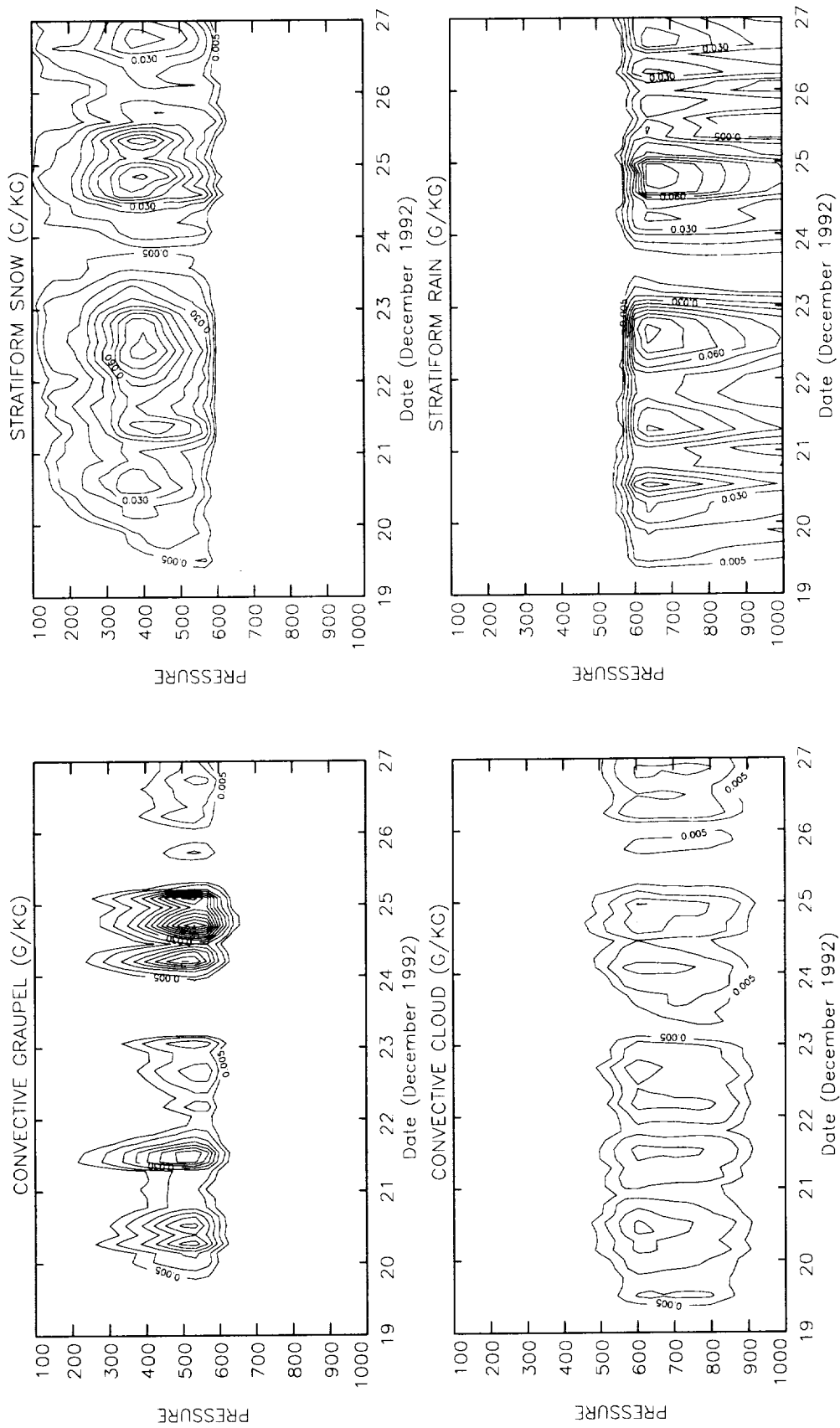


Fig. 23. Domain-averaged (a) graupel and cloud water mixing ratios (g kg^{-1}) in convective regions, and (b) snow and rain mixing ratios (g kg^{-1}) in stratiform regions for case C512.

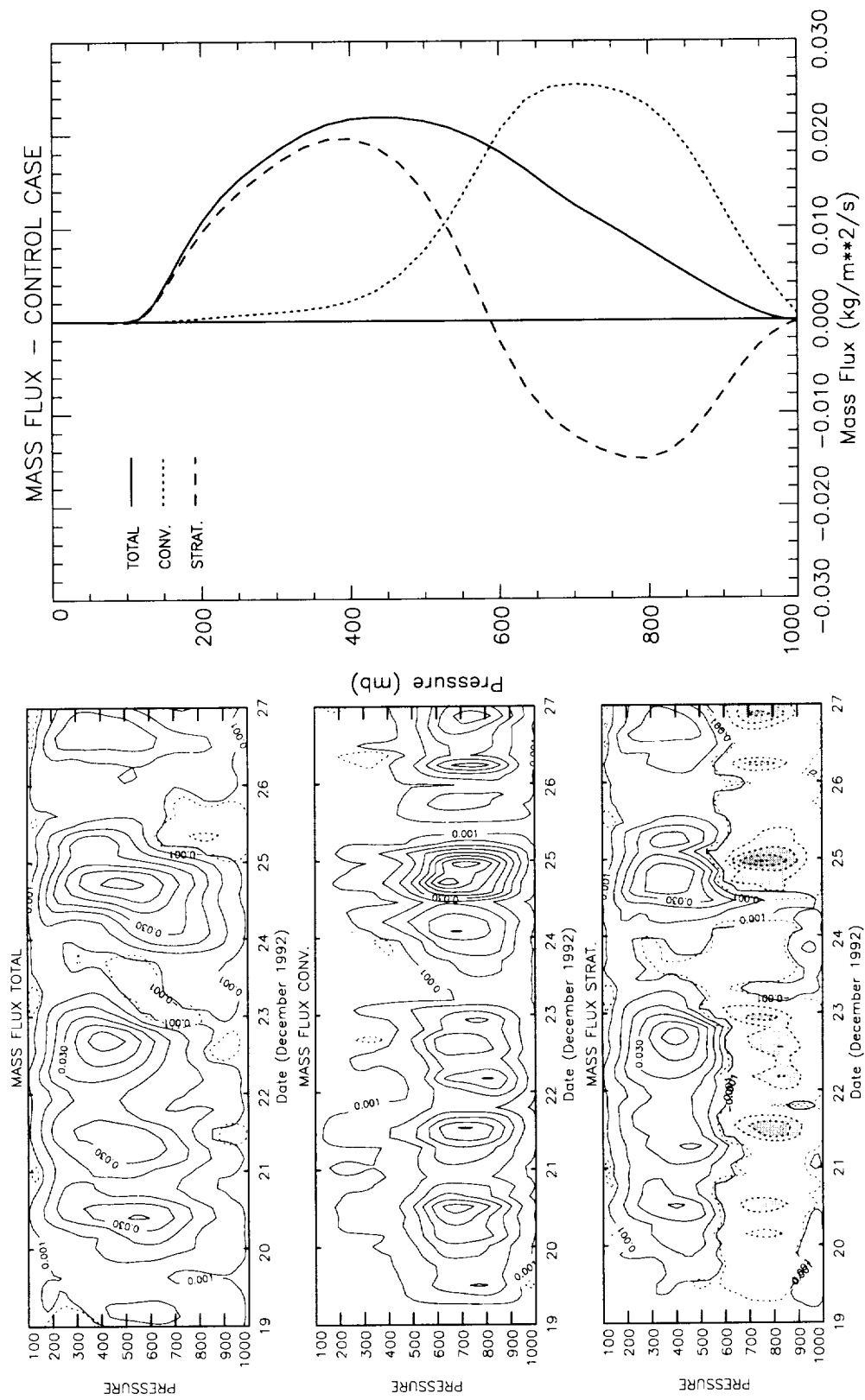


Fig. 24. (a) Domain-averaged, and (b) mean profiles of the total, convective, and stratiform mass fluxes ($\text{kg m}^{-3} \text{s}^{-1}$) for case C512.

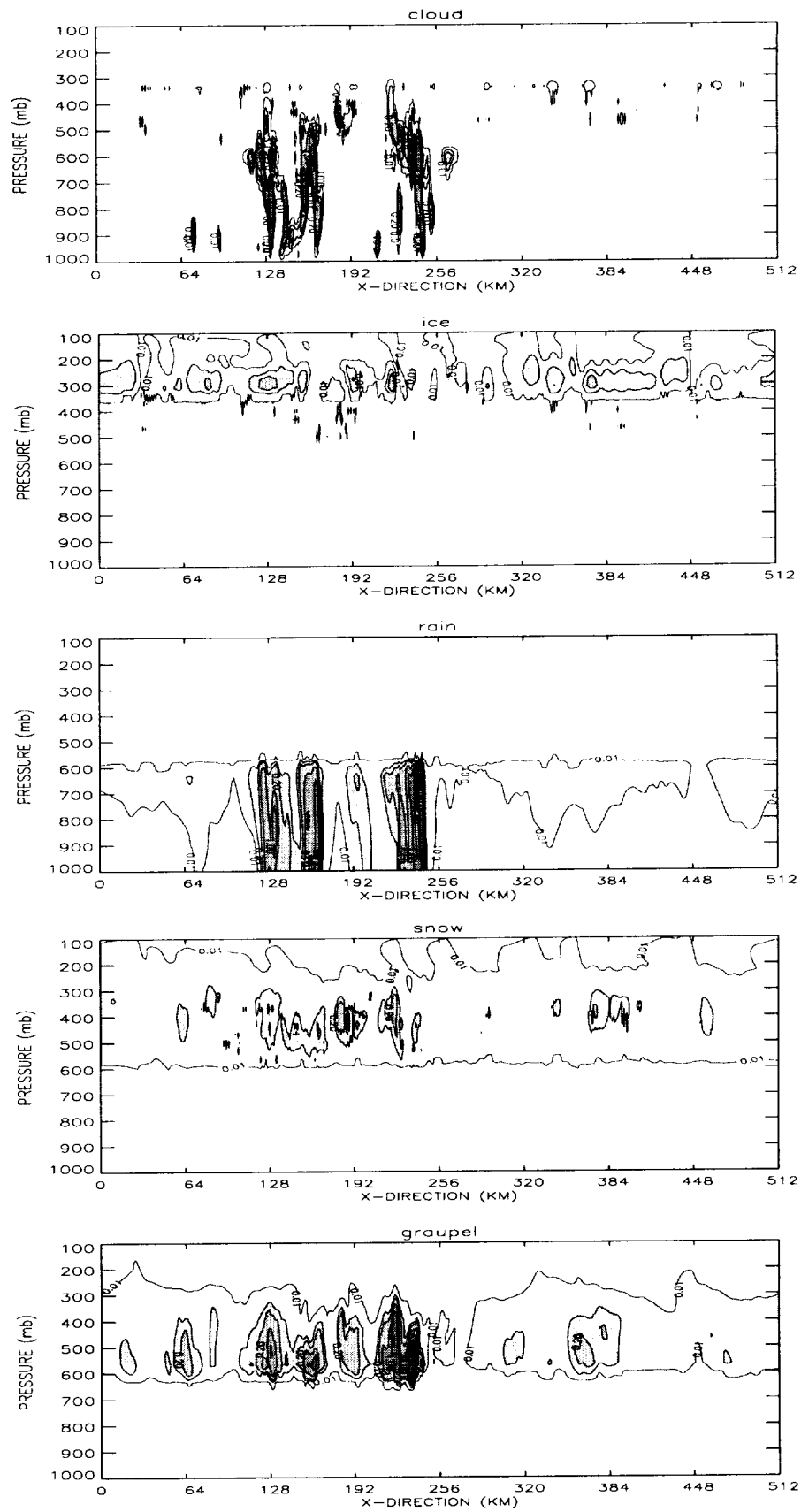


Fig. 25. Cross-sectional hydrometeor mixing ratio field contours (g kg^{-1}) for case C512 at 143 hours. The contour intervals are 0.01, 0.1, 0.2, 0.5, 1.0, 2.0, 5.0, and 10.0 g kg^{-1} .

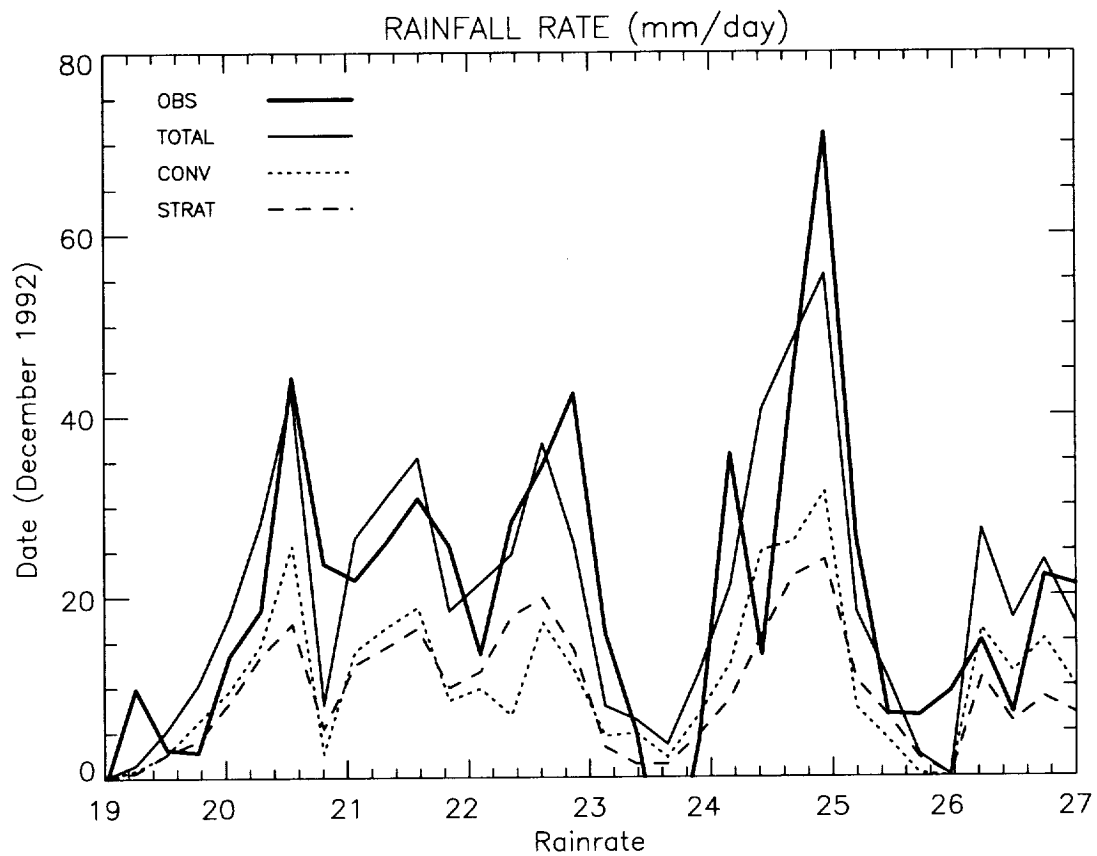


Fig. 26. Observed and domain-averaged simulated total, convective, and stratiform surface rainfall rates (mm day^{-1}) for case C512.

CONTROL CASE	Total Rainfall (mm)
Observed	160.8
Total	161.1
Convective	86.1 (53.3%)
Stratiform	75.5 (46.7%)

Table 7. Domain-mean total, convective, and stratiform surface rainfall (mm) and convective/stratiform percentage for case C512.

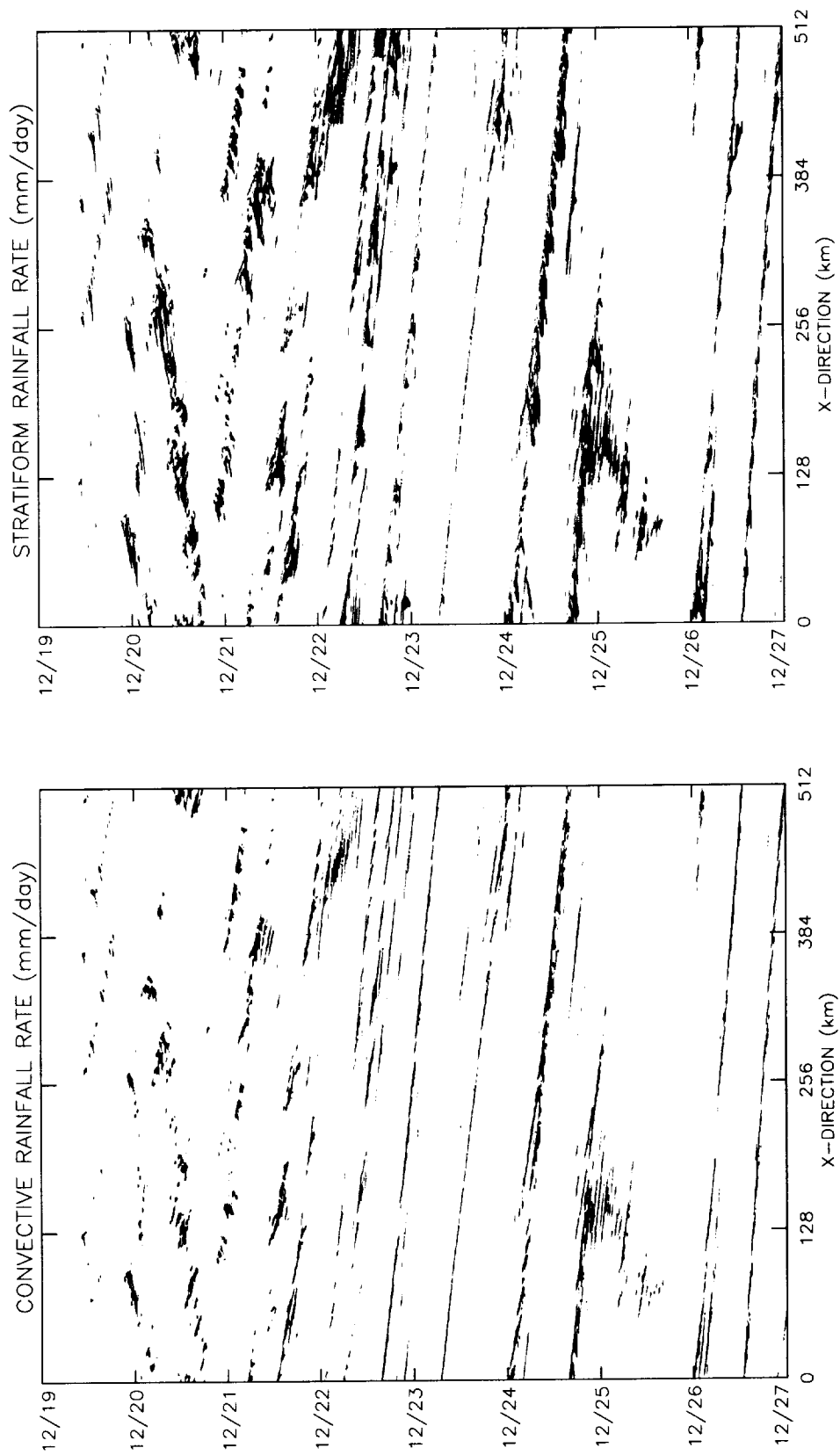


Fig. 27. X-T cross sections of rainfall rates greater than 1 mm/day for (a) convective, and (b) stratiform regions for case C512.

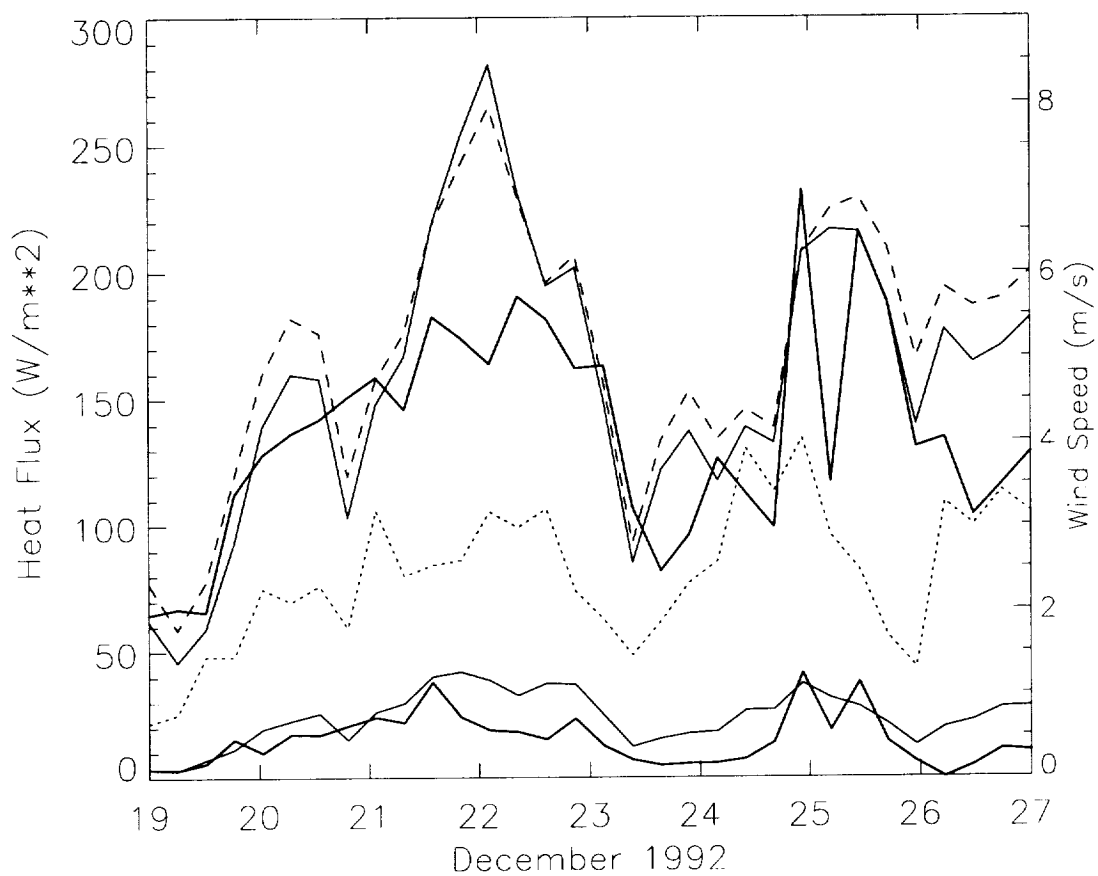


Fig. 28. Domain-averaged plots of observed (thick solid lines) and simulated (thin solid lines) latent (upper curves) and sensible (lower curves) heat flux (left scale; W m^{-2}), and mean wind speed (dashed line), and wind speed standard deviation (dotted line) at the surface (right scale; m s^{-1}) for the control case C512.